Bioinspired chromotropic ionic skin with in-plane strain/temperature/pressure multimodal sensing and ultrahigh stimuli discriminability

Heng Zhang[1], Haomin Chen[1,2], Jeng-Hun Lee[1], Eunyoung Kim[1], Kit-Ying Chan[1,3], Harun Venkatesan[1], Miracle Hope Adegun[1], Okikiola Ganiu Agbabiaka[1], Xi Shen[1,3]*, Qingbin Zheng[4], Jinglei Yang[1,5]*, and Jang-Kyo Kim[1,6]*

H. Zhang, H. Chen, J.H. Lee, E. Kim, Prof. X. Shen, Prof. Q.B. Zheng, Prof. J.L. Yang, Prof. J.K. Kim

[1] Department of Mechanical and Aerospace Engineering, The Hong Kong University of Science and Technology, Clear Water Bay, Kowloon, Hong Kong, China.

[2] Department of Materials Science and Engineering, KAIST Institute for the Nanocentury, Korea Advanced Institute of Science and Technology (KAIST), Daejeon 34141, Korea.

[3] Department of Aeronautical and Aviation Engineering, The Hong Kong Polytechnic University, Hung Hom, Kowloon, Hong Kong, China.

[4] School of Science and Engineering, The Chinese University of Hong Kong, Shenzhen, Guangdong 518172, China.

[5] HKUST Shenzhen-Hong Kong Collaborative Innovation Research Institute, Futian, Shenzhen, China

[6] School of Mechanical and Manufacturing Engineering, University of New South Wales, Sydney, NSW 2052, Australia

E-mail: xi.shen@polyu.edu.hk (X. Shen); maeyang@ust.hk (J.L. Yang); mejkkim@ust.hk (J.K. Kim)

Keywords: ionic skin, multimodal sensing, chromotropic iontronics, hybrid mechanism, stimuli discriminability.

Electronic skins mimic multimodal sensing capabilities of various tactile receptors in natural skin. Herein, a stretchable chromotropic ionic skin is rationally designed to simultaneously detect and decouple multiple stimuli, including in-plane strain, temperature and pressure. The mutually-discriminating trimodal ionic skin consists of mechanochromic, thermoresistive and triboelectric layers that individually function as strain, temperature and pressure sensors, respectively. These three distinct capabilities are integrated into the ionic skin which demonstrates highly sensitive responses to selective external stimuli while upholding high insensitivity to unwanted ones. The structural colors derived from mechanochromic photonic crystals of magnetic Fe_3O_4@C nanoparticles respond to strains by color-switching in

the full visible spectrum, exhibiting appealing potential in interactive stress visualization. The temperature detection with an exceptional sensitivity of 20.44 %/ °C is enabled by the thermoresistive effect of ionic hydrogel, while oriented polymer chains embedded in the hydrogel decouple temperature from extraneous stimuli. The multilayer structure consisting of an ionic hydrogel film, a wrinkle-patterned PDMS film with gradient modulus design and a CNT/PDMS electrode displays an extraordinary triboelectric effect with a strain- and temperature-insensitive pressure sensing capability. The chromotropic ionic skin facilitates simultaneously accurate measurements, high discriminability and quantitative mapping of complex stimuli, offering new insights into emerging E-skins.

1. Introduction

Natural skin sensory systems equipped with thermoreceptors and mechanoreceptors can detect and differentiate complex stimuli from the surrounding environment, such as strain, vibration, pressure and temperature.[1-4] Artificial electronic skins (e-skins) that can mimic human skin sensory functions have attracted tremendous attention for their revolutionary applications in the emerging fields of biomimetic prosthetics,[5, 6] humanoid robotics,[7, 8] human-machine interface and artificial intelligence.[9-12] E-skins are designed to translate external mechanical and thermal stimuli into detectable resistance, capacitance or voltage signals. In particular, state-of-the-art flexible e-skins aspire to simultaneously perceive more than one physical stimulus, such as pressure and temperature,[13, 14] strain and temperature,[15, 16] and strain and pressure,[17, 18] by means of innovative material properties like thermoelectric[19-21], ferroelectric[22, 23], piezoelectric and triboelectric[24] effects as well as structural engineering such as micropyramids,[25] microridges[26] and hierarchical patterns.[20] Despite these thriving advances in bimodal sensing,[27] developing a multimodal sensor capable of measuring more than two stimuli in a single unit is still a considerable challenge.[28-31] Multimodal sensing functions have been realized by integrating different sensors into one

sensing network through the layer-by-layer geometry design.[14, 19, 29, 32, 33] Each sensor exhibits a distinctive response to a specific stimulus, namely, the temperature-sensing layer in the temperature/pressure bimodal sensor presents pressure insensitivity, or vice versa.[19] Nevertheless, the multimodal sensors containing different functional sensory layers tend to exhibit inescapable mutual interference while requiring complicated device integration.[29] A preferred strategy for developing multimodal sensors with good interference immunity is therefore to rationally integrate multiple sensing principles such as, piezoresistive, piezocapacitive, thermoresistive, triboelectric, mechanoluminescent and mechanochromic effects, in a single sensory unit.[13, 18, 24, 31, 34-39]

The mechanochromism has been exploited to visualize mechanical stimuli with colorimetric changes for application in sensors and display devices.[40-44] For example, structural-colored materials integrated with intrinsically elastic substrates exhibit a reversible color-switching feedback in response to tensile and compressive forces.[45, 46] In addition, sensing materials with a thermoresistive effect, such as graphene oxide, carbon nanotubes (CNTs) and ionic hydrogels, are widely adopted to convert thermal fluctuations and temperature gradients to electrical signals.[47-53] Among them, ionic hydrogels that mimic the ion transduction of human somatosensory functions are an ideal candidate for a thermoresistive sensor due to their human tissue-like mechanical strength, biocompatibility, flexibility and multi-responsive behaviors.[18, 54, 55] Despite these pioneering achievements, however, it remains highly demanding to design sensitive temperature sensors capable of distinguishing temperature from mechanical stimuli in a single unit. In particular, completely eliminating interferences within the unit arising from different external stimuli is a nontrivial challenge for next-generation e-skins.

Bioinspired by the somatosensory functions of human skin and the structural color of panther chameleon skin,[43] this work, for the first time, is dedicated to developing a novel flexible chromotropic ionic skin that simultaneously detects and discriminates tensile strain,

temperature and pressure stimuli by means of the mechanochromic, thermoresistive and triboelectric sensing principles, as presented in Figure 1a. The arrayed ferroferric oxide-carbon (Fe_3O_4@C) core-shell magnetic nanoparticles with a mechanochromic photonic crystal structure were fast responsive to external force via interactive color switching. The structural-colored arrays embedded in the gelatin and polyvinyl alcohol (PVA) matrix acted as temperature-insensitive strain sensing elements with bright color reflection in the full visible spectrum from violet to red. In addition, the temperature-sensitive ionic hydrogel possessed an aligned polymer chain structure facilitating an ultrahigh temperature sensitivity of 20.44 %/°C in a wide range from 0 to 50 °C, thanks to their thermoresistive effect. Its extremely low strain sensitivity of 0.3 in gauge factor (GF) and intrinsic pressure insensitive properties mean that the temperature was easily decoupled from the mechanical stimuli by signal separation. The triboelectric structure of the multimodal sensor that consisted of a wrinkle-patterned polydimethylsiloxane (PDMS) friction layer with gradient modulus and a CNT-based elastic electrode enabled detection of voltage output, giving rise to strain-unperturbed and temperature-insensitive pressure sensing. On the whole, the integrated chromotropic ionic skin exhibited excellent strain/temperature/pressure multimodal sensing and stimuli discriminability through measuring the reflectance wavelength, resistance and voltage signals. The array of 4 × 4 multimodal sensors manifested accurate spatial mapping of decoupled tension, pressure and temperature stimuli, which may contribute to future development of interactive e-skin systems.

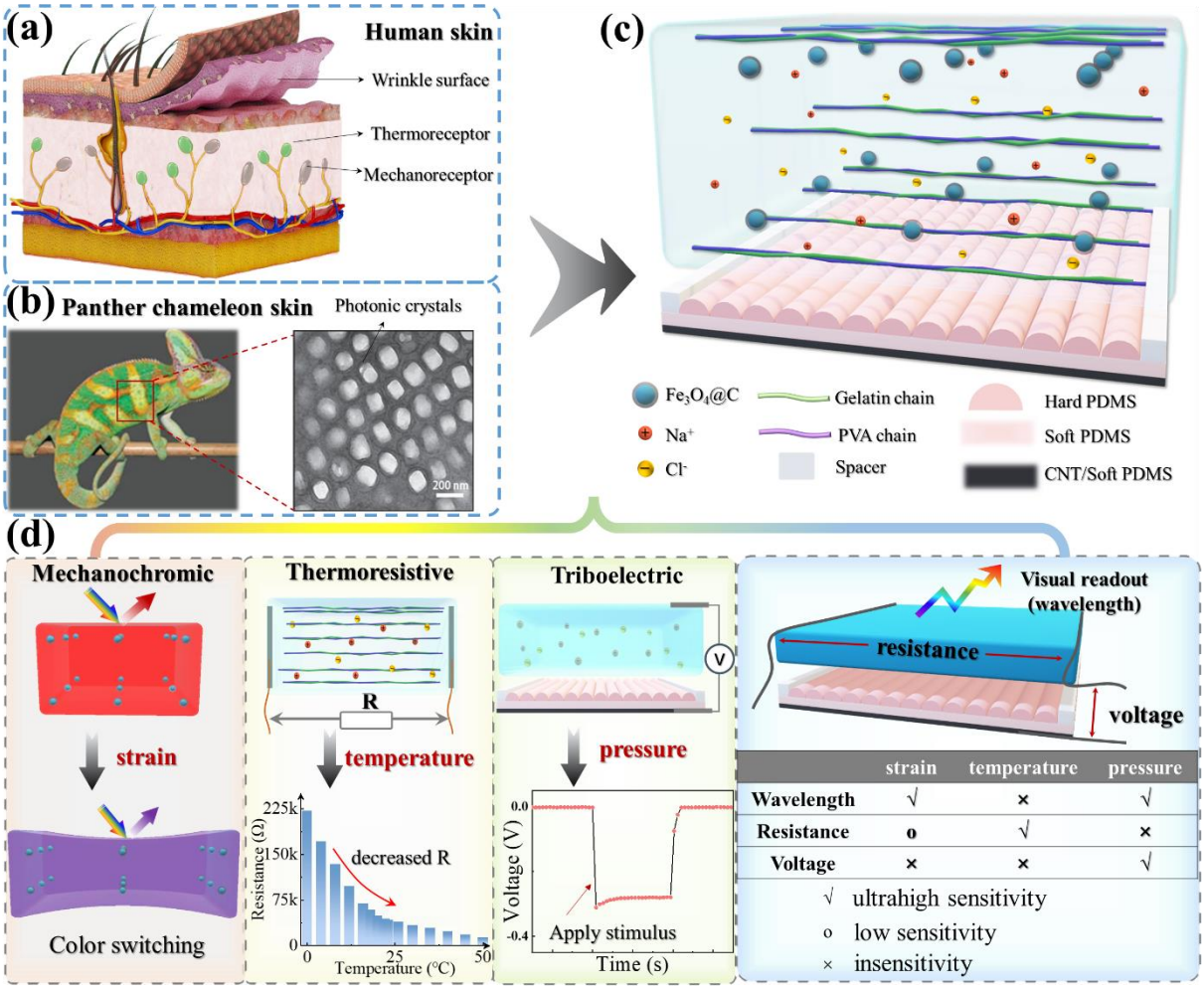

Figure 1. Illustrations of chromotropic ionic skin. (a) Schematic diagram of the human skin sensory system equipped with mechanoreceptor, thermoreceptor and wrinkle surface. (b) Panther chameleon skin with a photonic crystal nanostructure. This image is reprinted and adapted with permission under a Creative Commons CC-BY license from ref (43). Copyright 2015 Springer Nature.[43] (c) Schematic of the chromotropic ionic skin structure. (d) Conceptual representation of integrated mechanochromic, thermoresistive and triboelectric sensing mechanisms by means of the strain-sensitive wavelength, temperature-sensitive resistance and pressure-sensitive voltage signal, respectively.

2. Results and Discussion

2.1 Synthesis and characterization of multi-response chromotropic ionic skin

The chromotropic ionic hydrogel films containing aligned polymer chains and photonic

crystal particle arrays were fabricated with the aid of driving forces arising from the external magnetic field and directional freezing. Typically, magnetic core-shell Fe_3O_4@C nanoparticles were first synthesized through high-temperature ferrocene hydrolysis. The spherical cluster with a size of 130 nm has dozens of primary magnetite crystallites (of diameter 9 nm) in the inner core and an outer carbon shell (of diameter 15 nm), as shown in Figure 2a. Subsequently, ionic hydrogels were prepared using gelatin-based monomers capable of polymerization at low temperatures and containing abundant amine and amide functional groups, as verified by the peaks at ~3271 and 1620 cm^{-1} in the Fourier transform-infrared (FT-IR) spectra (Figure 2b). These functional groups acted as the surfactant stabilizer for improved dispersion of magnetic nanoparticles in the hydrophilic solvents, as proven by the Zeta potential comparison between the dispersions with and without gelatin monomers (Figure S1). Even after 2 hours of storage under the external magnetic field, the bright structural color of the Fe_3O_4@C/gelatin solution was well maintained, and its Zeta potential value presented only a marginal variation from -52.6 to -40.3 mV, implying significant benefits of the functional groups in the fabrication of chromotropic films. Another polymer, PVA, was then introduced into the gelatin matrix to form double networks through physical and chemical interactions so as to mitigate the brittleness of the single gelatin network (Figure 2c, Figure S2). The presence of PVA monomers significantly enhanced the stretchability of hybrid films while a moderate compressive modulus of 0.207 MPa was obtained by controlling the mass ratio of gelatin to PVA at 50:50. The same mass ratio was employed for further optimization of ion concentration and polymer chain structures unless otherwise specified.

After vigorously mixing and degassing the precursors including gelatin, Fe_3O_4@C, PVA, NaCl salts and glutaraldehyde (GA) in a sonicator, the homogeneous solution was injected into a Teflon mold which was lined with a magnet to construct the external magnetic field and connected to the cryogenic source at the bottom. The dispersed magnetic nanoparticles were assembled into the photonic crystals with a highly ordered array structure under the built

magnetic field, while the gelatin/PVA polymer monomers were crosslinked to form oriented chains with the aid of directional freezing (Figure 2d). The morphologies of the highly oriented gelatin/PVA chains were noted by the top and sectional scanning electron microscopy (SEM) images of unidirectional microchannels prepared through freeze-drying (Figure 2e-f). The SEM images of the nanoparticles embedded in the polymer matrix revealed a non-close-packed arrangement, as shown in Figure 2g-h. The cross-sectional SEM image of the hydrogel indicated an equivalent center-to-center distance of 450 nm in the ordered periodic structure (Figure S3). The photonic crystals in the hydrogel film were intended for temperature-insensitive strain sensing based on the mechanochromic mechanism, while the well-aligned polymer chains were designed for discriminable sensing of temperature stimulus based on the thermoresistive mechanism.

According to the triboelectric mechanism of the contact separation mode, an additional interference-free pressure sensor was built using an intermediate friction layer and a bottom elastic electrode along with a chromotropic hydrogel which acted as the top electrode (Figure 1c). Specifically, the friction layer is made of a wrinkle-patterned PDMS topological structure with an amplitude of 250 μm, (Figure 2i) and a 50 μm thick PDMS supporting film (Figure 2j). The PDMS assembly was designed to feature a gradient modulus across the hard semi-cylinder (with a high modulus of 2.44 MPa) on top and the soft substrate (with a low modulus of 0.312 MPa, Figure S4) underneath it, resulting in an uneven strain distribution under tension and therefore an almost constant contact area with the top electrode at a given pressure regardless of applied in-plane tension. A 150 μm thick CNT/PDMS composite layer (with a modulus of 0.497 MPa) was spin-coated to form a soft substrate (Figure 2j) in the bottom, serving as the back electrode of the patterned PDMS. The multilayer structure was finally encapsulated using Ecoflex films to prevent evaporation of water in the ionic hydrogel for improved long-term stability (Figure S5). The detailed compositions and molecular structures of different functional layers are summarized in Table S1. In the following, the individual sensing mechanisms are

discussed followed by their stimuli discriminability and collective responses towards multiplex stimuli.

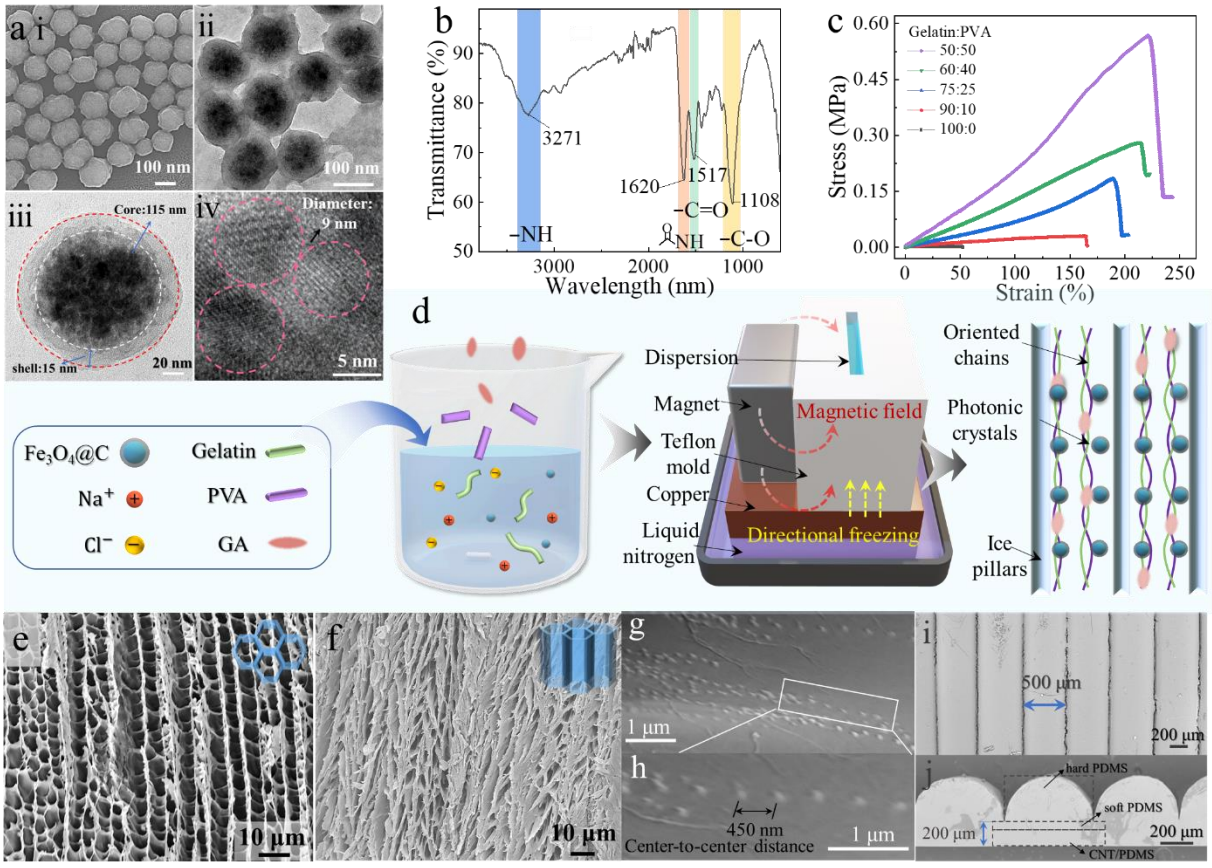

Figure 2. Morphologies and design of the chromotropic ionic skin. (a) <i> SEM image of the Fe_3O_4@C magnetic nanoparticles of 130 nm in average diameter; <ii> low and <iii> high magnification TEM images of Fe_3O_4@C nanoparticles showing the Fe_3O_4 core (of 115 nm in diameter) and C shell (of 15 nm in wall thickness); <iv> high-resolution TEM image of primary magnetite crystallites (of 9 nm in diameter). (b) FT-IR spectrum of gelatin. (c) Tensile strain-stress curves of the gelatin/PVA hydrogels with varying mass concentrations from 100:0 to 50:50. (d) Fabrication process of the chromotropic ionic hydrogels through synergistic driving force of external magnetic field and directional freezing. (e) Top and (f) cross-sectional SEM images of freeze-dried gelatin/PVA hydrogels showing the oriented polymer chains. (g) Low and (h) high magnification SEM images of the Fe_3O_4@C nanochains embedded in the freeze-dried polymer matrix, indicating a non-close-packed arrangement. (i) Top view and (j) cross-

sectional SEM images of the wrinkle-patterned friction layer and bottom CNT/PDMS elastic substrate.

2.2 Mechanochromic mechanisms towards interactive strain sensing

When the external magnetic field was applied to the dispersed magnetic nanoparticles, the interparticle electrostatic/steric repulsion force was balanced by the magnetic attraction force to assemble the randomly dispersed particles into a field-responsive periodic array.[56] After forming the photonic crystal structure in the polymerized gelatin/PVA matrix, the ionic hydrogel film exhibited bright structural color due to the diffraction of the incident light. As the incident light and the periodicity of the assembled particle array satisfied the Bragg condition, the light with a specific wavelength interfered and reflected, according to the following equation:[56]

$$\lambda=2d\times n_{average} \qquad (1)$$

where λ represents the reflective wavelength, d is the center-to-center distance between adjacent nanoparticles, and $n_{average}$ refers to the effective refractive index of the material. As the reflective wavelengths of solvent and polymer system of the chromotropic film remained constant, its reflective wavelength is principally governed by the center-to-center distance of the non-close-packed colloidal crystal arrays. This means that an effective strategy for obtaining different structural colors is to adjust the diameter of magnetic nanoparticles. Figure 3a-b reveals that by employing magnetic nanoparticles with diameters ranging from 130 to 250 nm, it was possible to obtain a series of chromotropic films with distinct initial colors, including violet, blue, green, yellow, orange and red, covering the entire visible spectrum from 430 to 680 nm. The wide coverage of visible spectrum allowed us to choose different initial colors depending on the external loading conditions (e.g., tension or bending) for achieving a maximum sensing range.

For in-plane strain sensing, the freestanding chromotropic ionic film displaying the initially

red color was selected for further experiments. In the strain sensitivity experiments, it was demonstrated that the structural color of the chromotropic ionic film underwent gradual color switch from red to violet as the applied strain was increased from 0 to 110% (Figure 3c and Figure S6). The corresponding reflective wavelength shifted from 680 to 430 nm during elongation, as indicated by the reflectance spectra in Figure 3d. The color switch during multiple stretching/releasing cycles was fully reversible and repeatable (Figure 3e), demonstrating the durability of the chromotropic ionic hydrogel. Upon stretching in the longitudinal direction, the thickness of the film along the observation direction was reduced due to the Poisson effect, leading to a reduction in center-to-center distance, *d*, between the neighboring nanoparticles. As a result, the reflective wavelength, λ, also decreased approximately linearly with increasing applied strain, which can be modeled by Equation S4 and Figure 3f. The highly linear λ_{max} vs strain plot with an R-squared of 0.986 across the full visible range (Figure 3g) is ascribed to the large spacing between the adjacent nanoparticles. Such a linear reflection-strain relationship plays an essential role in strain sensing and decoupling temperature response from the multiple stimuli (Equation S14).

To examine the mechanochromic response of the chromotropic ionic film to a bending strain, a freestanding, violet, flat film was prepared which was attached to the surface of a polyethylene terephthalate substrate. When the assembly was loaded in bending, the central part of the film was subjected to a compression on its concave surface and a tension on the convex side (Figure S7) along the longitudinal direction (Figure 3h). Consequently, the thickness of the film increased due to the Poisson effect, resulting in the red-shifted reflective wavelength peaks (Figure 3i and Equation S5). The structural color of the bent film changed nonuniformly, ranging from red in the center to blue at the edges, a reflection of the nonuniform stress distribution under lengthwise bending. The color distribution matched remarkably well with the stress distribution determined from the finite element analysis (Figure 3j), demonstrating potential application of the chromotropic ionic film as a stress mapping sensor.

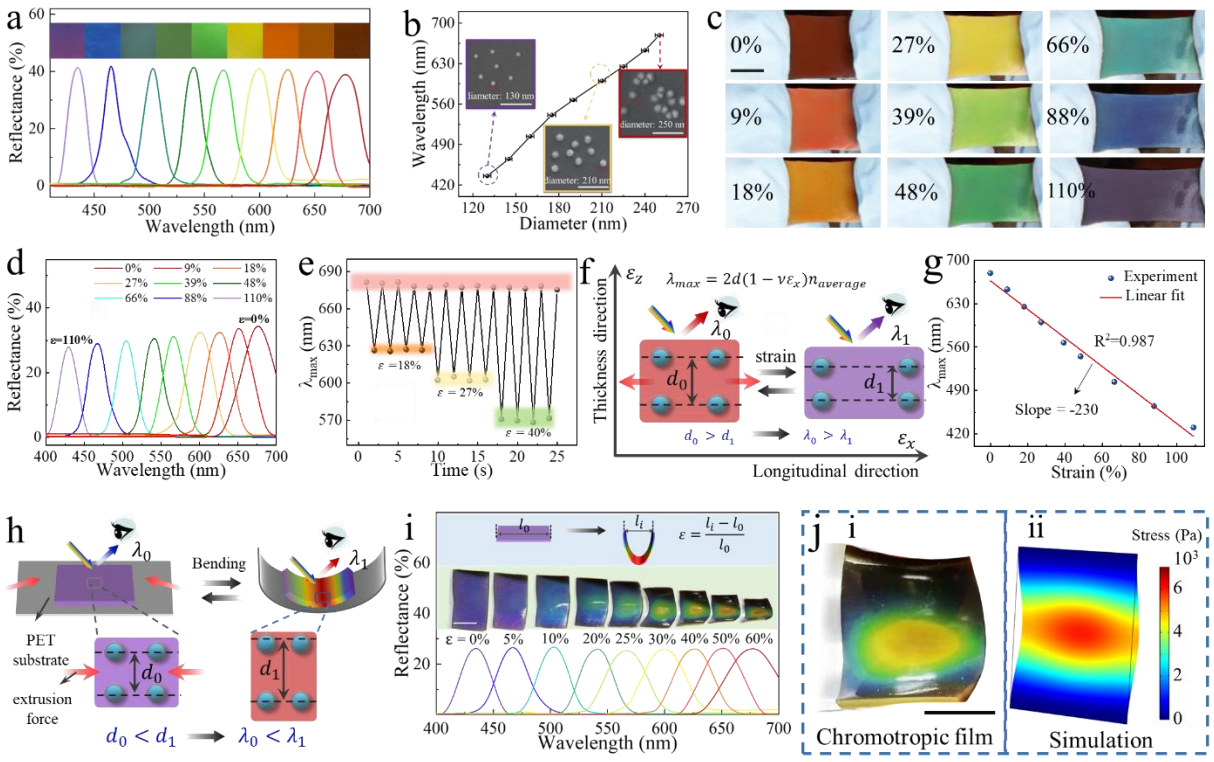

Figure 3. Mechanochromic properties for interactive strain sensors. (a) Chromotropic ionic film with different initial colors ranging from violet to red and corresponding reflectance spectra. (b) Relationship between reflective wavelength and diameter of Fe_3O_4@C nanoparticles. The morphologies of nanoparticles with diameters of 130, 210 and 250 nm are shown in inset SEM images (scale bar = 1 μm). (c) Evolution of structural colors of the initially dark red film when stretched to different strains ranging from 0 to 110% (scale bar = 1 cm). (d) Reflectance spectra of the initially dark red chromotropic film at different tensile strains from 0 to 110%. (e) Repeatability of λ_{max} at 18, 27 and 40% strains. (f) Schematic illustration of color switching behavior under tension. (g) Linear relationship between refractive wavelength peak (λ_{max}) and applied strain. (h) Schematic illustration of mechanochromic response to bending. (i) Reflectance spectra of the chromotropic ionic film with an initially violet color under different bending strains (in negative sense) on the concave side. The photographs in inset exhibit color changes of the film under bending strains from 0 to 60% (scale bar = 10 mm). (j) Nonuniform distributions of <i> structural color and <ii> simulated stress (in negative sense) on the concave surface of the bent film.

2.3 Thermoresistive sensing mechanisms towards temperature sensing

The thermoresistive behavior of the ionic hydrogel was utilized to monitor temperature stimuli. The ionic conductivity stems from free migration of the Na^+ and Cl^- ions in the hydrogel networks. Figure 4a presents Nyquist plots of the ionic films with different NaCl concentrations measured by the electrochemical impedance spectroscopy (EIS), proving the non-Faradaic process with no charge crossing the electrode-conductor interface.[57] The impedance of hydrogels obtained from the intercepts of EIS curves with the x-axis decreased with increasing NaCl concentration. The corresponding ionic conductivity initially rose rapidly, followed by an almost linear, slow increase against ionic concentration (Figure 4b). A further increase in NaCl concentration had little contribution to the ionic conductivity because of the formation of ion pairs or ion clusters which had no effect on accumulated ion mobility. The temperature-dependent performance of the ionic hydrogel was characterized by the resistance measured at different temperatures, as shown in Figure 4c. The resistance decreased exponentially from 221.5 to 16.5 kΩ as the temperature increased from 0 to 50 ℃ owing to the acceleration of ionic mobility, indicating ultrahigh sensitivity to temperature. The experimental data fitted well with the resistance-temperature function derived from the Arrhenius law (Equation S7). For practical application of the temperature sensor, the relative resistance change ($\Delta R/R_0$) was calculated, and the temperature coefficient of resistance (TCR) was used as a measure of sensitivity:

$$\mathrm{TCR} = (\Delta R/R_0)/\Delta T \quad (2)$$

where ΔR refers to the resistance change upon temperature variation, ΔT, and R_0 is the resistance value at 23 ℃, thus TCR remains zero at 23 ℃. The exponential curve over the whole working range of 0-50 ℃ was divided into two linear regions, namely, a low-temperature region (0-20 ℃) with a high TCR of 20.44 %/℃ and a high-temperature region (20-50 ℃) with a low TCR of 2.54 %/℃, as shown in Figure S8.

The temperature-dependent relative resistance changes of ionic hydrogels with different

NaCl concentrations are manifest in Figure 4d-e. The slope of the curves decreased with elevating ion concentration, especially in the low-temperature region, indicating reduced temperature sensitivities with low TCR values. It follows then that high initial impedances arising from low NaCl concentrations are preferred for highly sensitive temperature sensors because of more appreciable resistance drops with increasing temperature. Meanwhile, the resistance change with temperature should ideally be insensitive to in-plain strains so as to avoid signal crosstalk between temperature and strain.[1] The relationship between the strain sensitivity, i.e., GF, and the ion concentration is depicted in Figure 4f and Figure S9. The GF dropped sharply to 0.3 as the NaCl concentration increased to 0.2 M and did not change much with further increase in ion concentration. Therefore, to balance the demand for ultrahigh temperature sensitivity and strain insensitivity, an optimal NaCl concentration of 0.2 M was chosen for further study.

Another prominent feature of the designed chromotropic hydrogel film is the aligned polymer chains enabled by directional freezing, giving rise to an anisotropic structure[55] which had a positive effect on temperature sensing due to the boosted ionic conduction, as shown in Figure 4g. The TCR value of the aligned structure at low temperatures was 20.4%/°C, which is more than four times the random and perpendicular network counterparts, where the ion transportation in the aligned channels was much smoother than in the latter network structures. The drastic improvement in temperature sensitivity, TCR, accentuates the fascination arising from the rational design of directional structures for modulating ion transportation. Furthermore, even after more than 200 cycles of cooling (10 °C) and heating (40 °C), the relative resistance changes remained highly consistent (Figure 4h), a testament to excellent stability of the temperature sensor.

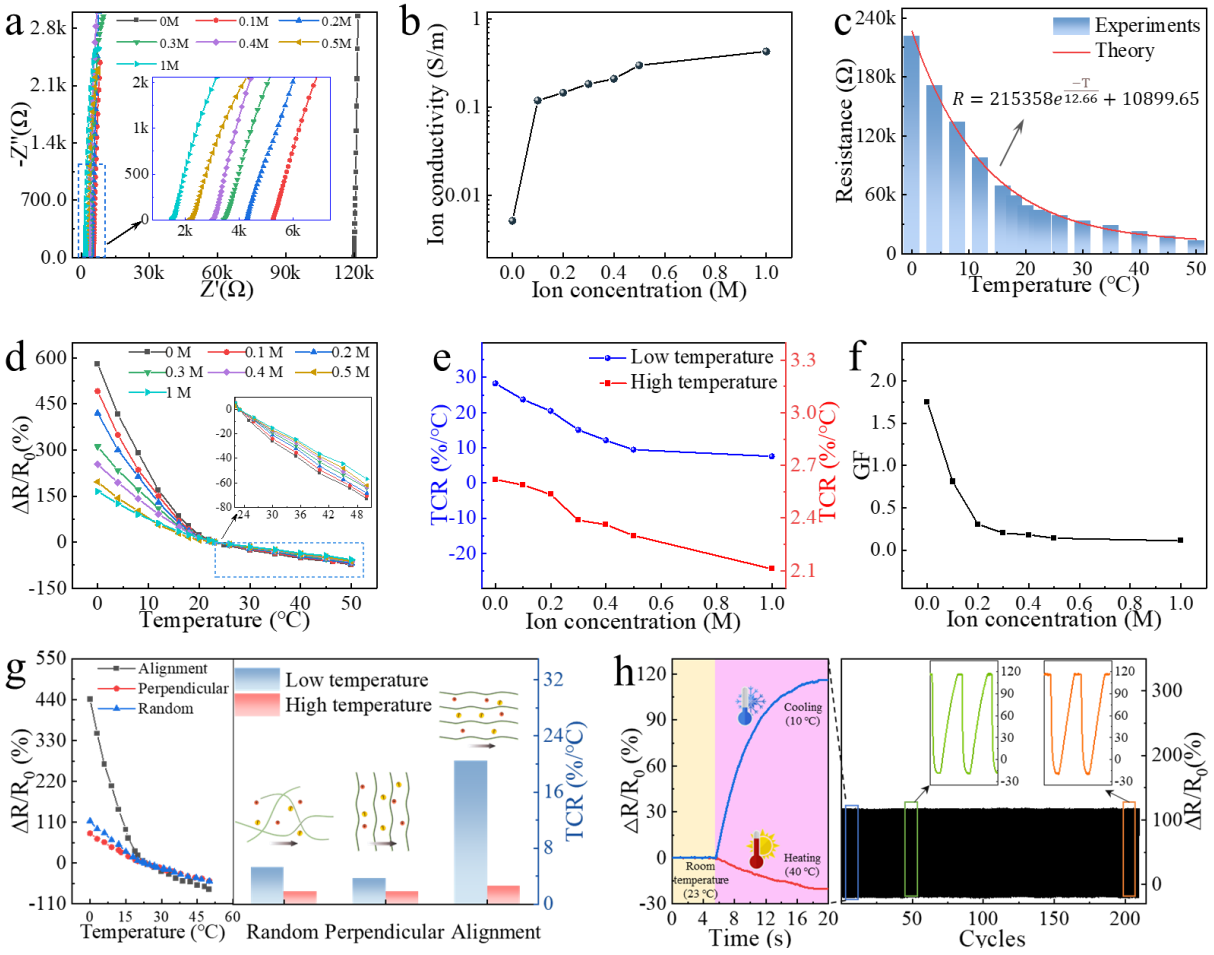

Figure 4. Thermoresistive response of the temperature sensor. (a) EIS Nyquist plots of the ionic films with different NaCl concentrations. (b) Calculated ion conductivities of ionic films with different NaCl concentrations. (c) Experimental resistance of the ionic film measured at different temperatures and the corresponding theoretical curve based on the Arrhenius law. (d) Relative resistance changes against temperature of the ionic films with different NaCl concentrations. (d) TCR values of the ionic films with different concentrations at low and high temperatures. (f) GF values of the ionic films with different NaCl concentrations. (g) Relative resistance changes verse temperature and TCR values of the aligned structure in the longitudinal and perpendicular directions and the random structure. (h) Relative resistance changes when the ionic film is subjected to cooling (10 ℃) and heating (40 ℃) cycles, showing highly stable performance after 200 cycles.

2.4 Triboelectric response of single-mode pressure sensor

The highly sensitive pressure sensor was implemented by constructing the triboelectric multilayer structure consisting of a chromotropic ionic hydrogel film (electrode), a wrinkle-patterned PDMS film (friction layer) and a CNT/PDMS elastic electrode (Figure S10). Its pressure sensing performance was described by the voltage output arising from the triboelectric effect in the contact/separation mode, as shown in the working principle (Figure 5a). When the ionic hydrogel film was pressed onto the patterned PDMS assembly, positive and negative charges were generated at the interface. The opposite ions were accumulated on the surface of two electrodes due to electrostatic induction, giving rise to a potential difference when the ionic hydrogel film and PDMS film were separated. Upon increasing pressure, both the elastic ionic hydrogel film and the protruding wrinkle pattern adaptively deformed, contributing to a larger contact area between the two surfaces, which was verified by the numerical simulation (Figure 5b) where the contact area quadrupled with increasing applied pressure from 0.5 to 5 kPa.

The increased contact area caused by the higher pressure in turn enhanced the triboelectric effect, resulting in a larger potential difference. The relationship between the pressure and measured voltage is shown in Figure 5c. The sensitivity of pressure sensing, S, was evaluated using the equation, $S=\Delta V/\Delta P$, where ΔV refers to the voltage change and ΔP is the applied pressure change. Therefore, the sensitivities were obtained, S_1=-528.0 V/kPa in the low-pressure range (0-2 kPa) and S_2=-63.7 V/kPa in the high-pressure range (2-9 kPa). Figure 5d presents the voltage output response to repeated loading and unloading cycles at different pressures ranging from 0.2 to 0.8 kPa, demonstrating high accuracy and reliability of the pressure sensor. A short response time of 44 ms, a recover time of 133 ms and an extremely low detection limit of 65 Pa are also shown in Figure 5e. The durability and robustness of the pressure sensor were evaluated using the long-term cyclic test. As plotted in Figure 5f, the output voltage signals obtained after 1000 cycles of contact/separation motion were consistent with the initial cycles thanks to the well-maintained interfacial adhesion among multilayers

(Figure S11), proving high stability of the sensor in the long-term practical application.

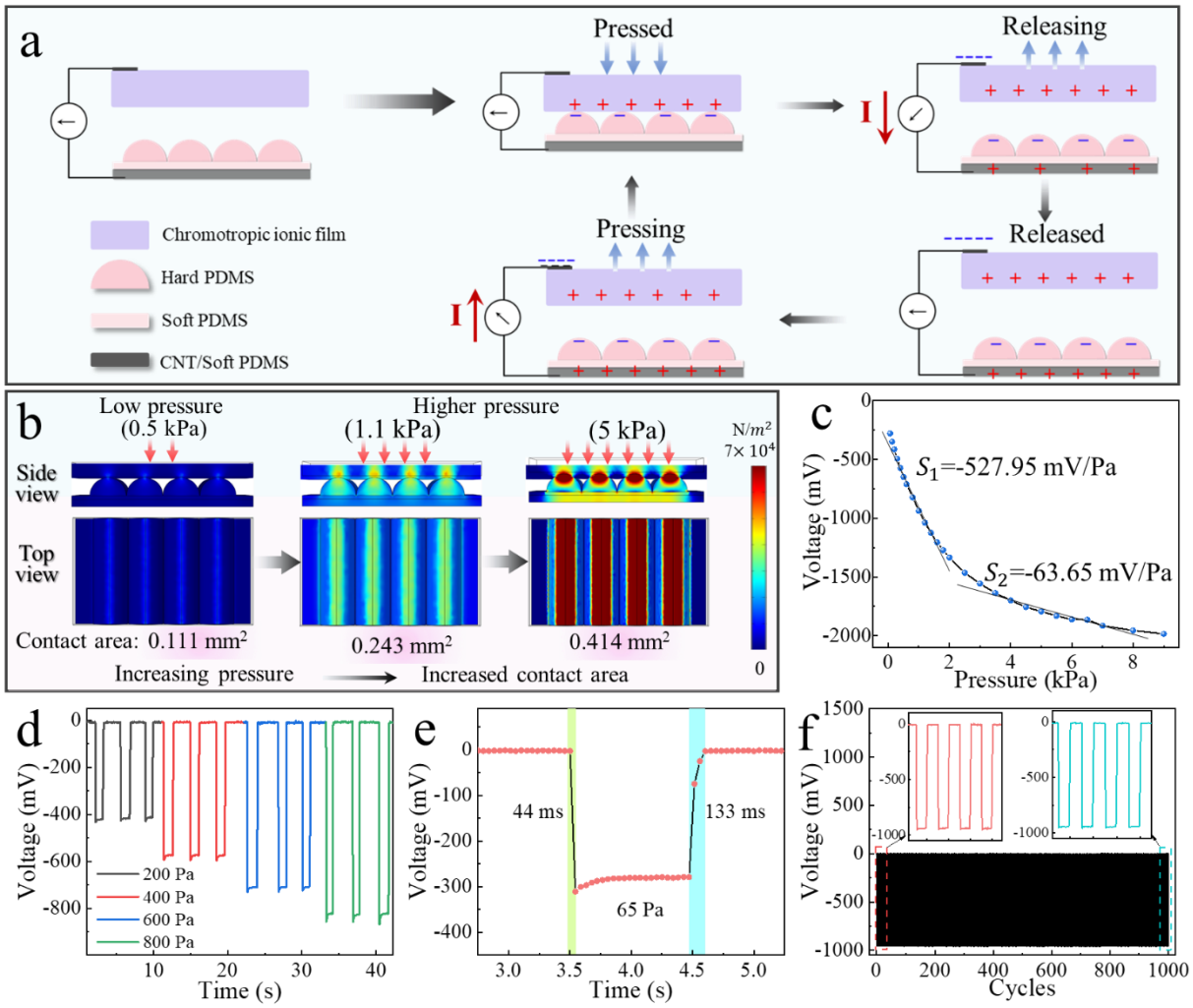

Figure 5. Sensing performance of the triboelectric pressure sensor. (a) Schematic diagram of the working principle of the triboelectric pressure sensor. (b) FEM simulation results of the increased contact area between the ionic hydrogel film and wrinkle-patterned friction layer upon increasing applied pressure. (c) Voltage change against pressure with two linear segments: a high sensitivity of -528.0 mV/Pa at 0-2 kPa and a low sensitivity of -63.7 mV/Pa at 2-9 kPa. (d) Pressure sensing performance under 200, 400, 600, and 800 Pa pressing/releasing cycle. (e) Detection and recovery behavior of the pressure sensor. (f) Repeatability and durability of the pressure sensor to 1000 loading/unloading cycles at 1 kPa.

2.5 Stimuli discriminability and application of multimodal sensor

The most distinctive characteristic of the current chromotropic ionic skin is its capability

to distinguish in-plain strain, temperature and pressure stimuli with negligible interferences among the responses to them. The functionalities of the sensor to simultaneously detect and distinguish multiple stimuli were explored by recording the reflectance wavelength, resistance and voltage signals when subjected to three different external stimuli. First, the chromotropic ionic film with an initially dark red color (at a wavelength of 680 nm) exhibited excellent dimensional stability with no color change when the temperature was altered between 0 and 50 °C, as shown in Figure S12, proving decoupling of temperature from in-plain strain. When the dark red color film was stretched to different in-plane strains up to 110% while simultaneously subjected to temperature variation between 10 and 40 °C, the wavelength change is presented in Figure 6a. The color-switching behavior due to stretching remained consistent regardless of different temperatures. In particular, there was high stability of color changes between dark red (680 nm) and violet (430 nm) in response to a full range of stretching/releasing cycles between 0 and 110% strain, independent of the applied temperature (Figure S13). Besides, the mechanochromic response of the sensor containing Fe_3O_4@C photonic crystals exhibited a decrease in reflectance wavelength upon pressure. The strain stimulus was isolated from the strain/pressure mixed stimuli by utilizing the spatial resolution of the mechanochromic film towards strain sensing. As the initially dark red film was subjected to a combination of 40% in-plane strain and pressure of ~500 Pa, the reflectance spectra upon applying/releasing the pressure were recorded. The dark red changed to light green (at wavelength of 567 nm) when stretched, as shown in Figure S14a. When the glass plate on the film was pressed using a tweezer, the reflectance wavelength in the region of the pressure source was reduced to a dark green color (at wavelength 528 nm), while the wavelength in the region surrounding it remained unchanged. This means that the pressure stimulus could be differentiated from the in-plane strain by means of color shifts in the pressure source region relative to the surrounding region. The net in-plane strain response was therefore obtained from the wavelength corresponding to the whole region after the release of pressure (Figure S14b).

The in-plane strain and pressure stimuli were applied simultaneously along with temperature variation to assess the insensitivity of the temperature sensor to unwanted interference from other stimuli. There were drastic reductions in resistance from 145 to 16.5 kΩ when the temperature varied from 10 to 50 ℃ without an in-plane strain stimulus, indicating its high sensitivity to temperature stimulus (Figure S15). When a tensile strain was applied at the same time, however, the resistance increased to a certain extent depending on the prevailing temperature: the higher was the temperature, the smaller was the increase in resistance (Figure S16). Interestingly, it is noted that the relative resistance changes, $\Delta R/R_0$, due to stretching to a constant 100% strain were consistently ≈ 0.3 at all temperatures applied (Figure S17). A similar behavior was observed when lower strains were applied to the temperature sensor, giving rise to proportionally consistent $\Delta R/R_0$ values of ≈ 0.24 and 0.12 at 80% and 40% strains, respectively. This interesting finding allowed us to modulate the influence of strain stimulus to decouple the required temperature information from the simultaneous temperature and extraneous strain stimuli. The details of the strain modulation are given by Equations (S9)-(S11) and Table S2 in Supplementary Information. Figure 6b presents the resistance values measured under 100% strain against temperature before and after modulation in comparison with the data obtained without strain stimulus, indicating the temperature sensor indeed possessing high strain insensitivity**.** In addition, the pressure-insensitive performance of the temperature sensor was assessed by measuring the resistance changes under different pressures. High pressure insensitivities of over 95% were achieved in the sensing range of 0-10 kPa owing to the optimized modulus, as shown in Figure S18. When the ionic skin was subjected to simultaneous temperature and pressure variations, the relative resistance change measured at a given temperature was almost constant regardless of pressure within the proposed working range (Figure 6c), signifying excellent pressure insensitivity.

The major functional challenge for pressure sensing lies with the stretching and

temperature variations leading to lower sensing accuracies, which was overcome by designing the wrinkle-patterned frictional layer with gradient modulus.[14] Its insensitivity to extraneous stimuli, such as strain and temperature, were experimentally validated by recording the voltage signals under different temperatures and strains coupled with pressure. The voltage variations against applied pressure ranging from 0 to 1.6 kPa were measured while different in-plain strains up to 80% were simultaneously applied (Figure 6d, Table S3). It is clearly seen that the pressure sensing performance was consistently excellent regardless of in-plane tensions. The voltage readings differed by only an average of 2% when subjected to strains ranging from 0 to 80%. The ultrahigh insensitivity performance of the pressure sensor to in-plane strains can be explained by the small contact area and uniform strain distribution enabled by the gradient modulus structure of the wrinkle-patterned layer. When the sensor was stretched to 100% strain under pressure, the top, high-modulus protruding wrinkle patterns forced the majority of applied strain to be taken up by the bottom low-modulus PDMS layer rather uniformly, while maintaining small contact areas with the ionic hydrogel film and therefore stable voltage outputs, as shown in Figure 6e and Figure S19. In contrast, the wrinkle patterns in the conventional pressure sensor with uniform modulus design deformed as much as the bottom layer, causing substantially increased contact areas with the ionic hydrogel film (Figure S19d) and thus interfering with the pressure sensing accuracy (Figure S19e). Figure 6f shows that there was a sizeable voltage drop of ~940 mV upon the application of a pressure 1 kPa, which was found to be insensitive to a simultaneous stretching/releasing cycles of 100% in-plane strain. This finding is notwithstanding the linear increase of resistance in the CNT/PDMS elastic conductive layer by almost 23% during stretching to 100% strain (Figure S20). It follows then that the constant contact area between the ionic film and wrinkle-patterned PDMS layer regardless of stretching enabled by the gradient modulus design was the predominant parameter that determined the strain-independent sensing performance of the triboelectric pressure sensor.[25] The interference-free pressure sensing from the simultaneous temperature stimulus

was explored by continuously recording the voltage outputs under temperature variations ranging from 10 to 40 °C, as shown in Figure 6g. The pressure sensor under a constant pressure of 1 kPa was subjected to different temperature environments, including ambient air (at 24 °C), cold water bath (at 10 °C) and warm water bath (at 40 °C). It is noted that the voltage output remained quite stable during the whole experiment. The lower temperature tended to marginally reduce the voltage output, and vice versa, due probably to the modified intrinsic impedance of ionic hydrogel at different temperatures.[14] However, the temperature interference was insignificant and had a minor effect on the overall pressure sensing performance of the triboelectric sensor.

Given the negligible interferences among three different responses of wavelength, resistance and voltage as discussed above, our chromotropic ionic skin exhibited an excellent capability of simultaneously monitoring the in-plane strain, temperature and pressure stimuli in real-time when compared with reported state-of-the-art multimodal sensors (Table S4). As the highlight of this work, the multiple stimuli sensing capability of the chromotropic ionic skin was further studied using a flexible sensor array with 4 × 4 pixels, as shown in Figure 6h <i>. Each unit in the array remained independent and electrically separated. The ionic skin array was attached to the palm of human hand, which was stimulated by applying complex in-plane strains when the palm performed a grasping action. In addition, a relatively heavy bottle containing hot water (of 5 g in weight, 45 °C) and a light bottle filled with cold water (of 3 g in weight, 10 °C) were placed on a unit each, introducing both temperature and pressure stimuli (Figure 6h <ii>). Under the simultaneous application of strain, temperature and pressure stimuli, the output signals of structural color wavelength, resistance and voltage of individual units were recorded. The structural colors of the array which were visible to human eyes were captured by photographing, and the maximum reflectance wavelength in each unit was recorded separately (Figure 6h <iii>) and combined to a 3D map, showing the highest bending stress (in negative sense) in the center of the grasped palm concave side (Figure 6i <i>). Simultaneously, the

distributions of temperature and pressure were depicted in the subsequent data analysis and visualization of the collected resistance and voltage responses (Figure 6i <ii>, <iii>). It is clearly seen that the sensor array was able to monitor independently and decouple from one another the simultaneously applied multiple stimuli including in-plane strain, temperature and pressure.

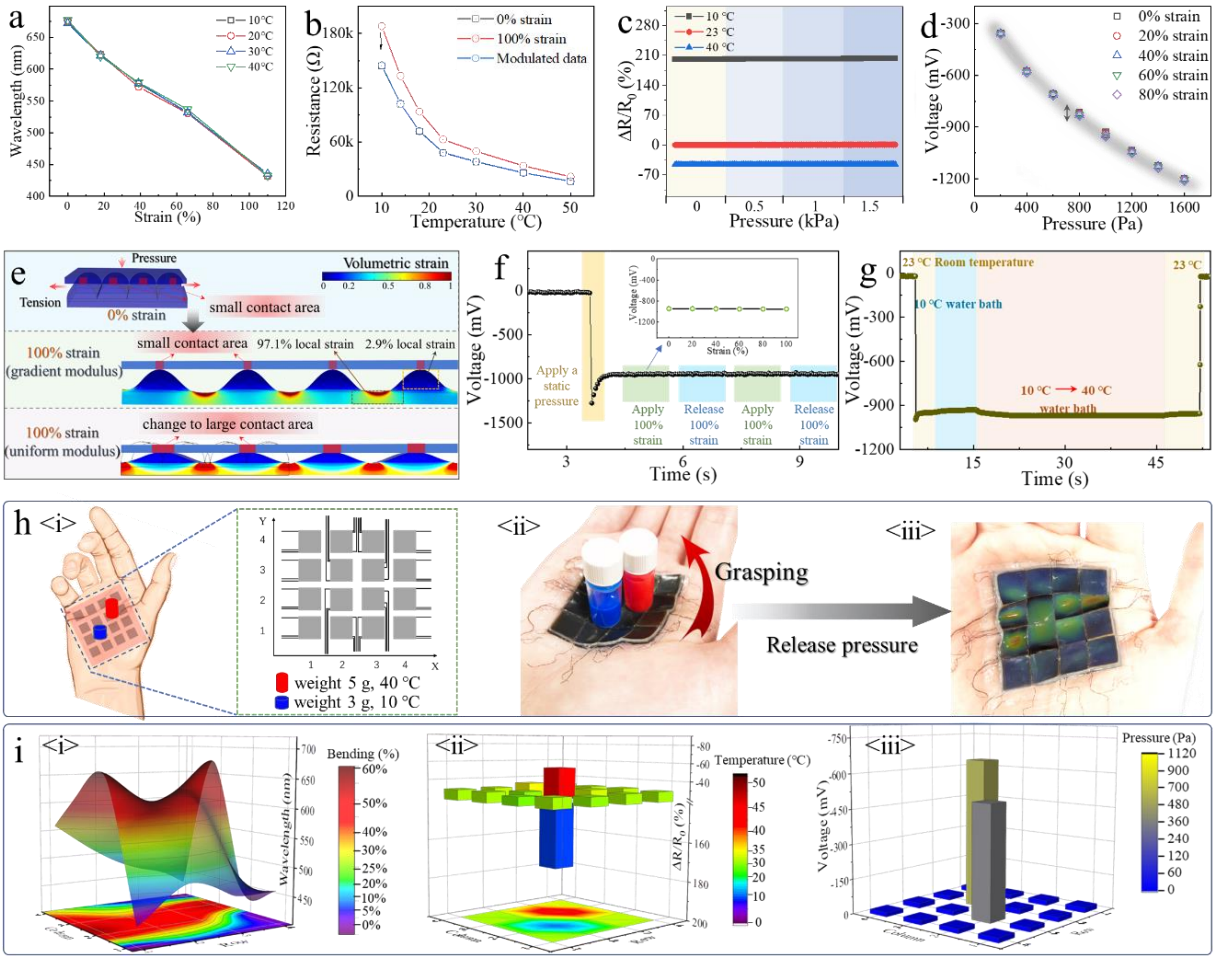

Figure 6. Signal discriminability of strain, temperature and pressure stimuli. (a) Reflectance wavelength of the structural-colored ionic skin stretched to 110% strain at different temperatures. (b) Resistance changes of the ionic skin temperature sensor when subjected to 100% in-plain strain with and without signal modulation. (c) Relative resistance changes of the ionic skin temperature sensor when subjected to simultaneously different temperatures and pressures. (d) Voltage responses of the pressure sensor to increasing pressure when different in-plain strains are applied simultaneously. (e) Contact area and volumetric strain distributions of

the wrinkle-patterned pressure sensors prepared with uniform modulus or gradient modulus PDMS when both pressure and 100% tensile strain are applied simultaneously. (f) Voltage changes of the pressure sensor in response to a constant pressure applied to the ionic skin, followed by stretching/releasing cycles of 100% strain. The inset figure indicates a very stable voltage signals during stretching at 0-100% strain. (g) Voltage output of the ionic skin when temperature is varied from 10 to 40 ℃. (h) <i> Schematic diagram and <ii> photograph of the sensor array attached to the human palm with glass bottles containing water with different weights and temperatures and grasping action. <iii> Photograph showing the changed structural color of the sensor array (initially violet) due to grasping. (i) <i> 3D map of the collected reflectance wavelengths, <ii> modulated relative resistance change, and <iii> voltage signals, showing the distributions of in-plane strain, temperature and pressure, respectively.

3. Conclusion

In summary, a mutually-discriminating, highly sensitive trimodal ionic skin is designed to simultaneously detect and decouple in-plane strain, temperature and pressure responses via multiple sensing principles of the mechanochromic, thermoresistive and triboelectric effects. The bright structural colors derived from photonic crystals exhibited fast color switches in the full visible spectrum in response to the in-plane strain stimulus. The non-closely arranged Fe_3O_4@C magnetic particle array embedded in the stretchable gelatin/PVA hydrogel matrix possesses a highly sensitive, linear, reversible, durable and temperature-insensitive strain sensing capability, with appealing potential to visualize interactive strain spatial distribution maps. The thermoresistive effect of the ionic hydrogel with aligned polymer chains facilitated an ultrahigh temperature sensitivity of 20.44%/℃ in a wide range from 0 to 50 ℃. Its decoupling from strain and pressure stimuli was made possible by signal separation based on the extremely low strain sensitivity and stable relative resistance variations at different temperatures. The strain-unperturbed and temperature insensitive pressure sensing of the

multilayer triboelectric structure possessed many useful merits, including a high sensitivity, a low detection limit of 65 Pa, a fast response speed of 50 ms and a stable operation for 1000 cycles, thanks to its gradient modulus design in the wrinkle-patterned friction layer. These three distinct capabilities manifest highly sensitive responses to selective external stimuli while maintaining high insensitivity to unwanted ones. The chromotropic ionic skin capable of accurate measurement and quantitative mapping of strain, temperature and pressure stimuli without interferences among them would find potential applications in the emerging area of human-machine interaction, prosthesis and robotics.

4. Experimental Section

The detailed experimental section can be found in the Supporting Information.

Supporting Information

Supporting Information is available from the Wiley Online Library or from the author.

Acknowledgements

This project was financially supported by the Research Grants Council (GRF Projects: 16205517, 16209917 and 16200720) and the Innovation and Technology Commission (ITS/012/19) of Hong Kong SAR. This work was also supported in part by the Project of Hetao Shenzhen-Hong Kong Science and Technology Innovation Cooperation Zone (HZQB-KCZYB-2020083). Technical assistance from the Materials Characterization and Preparation Facilities (MCPF) and the Advanced Engineering Material Facility (AEMF) at HKUST are appreciated.

Received: ((will be filled in by the editorial staff))

Revised: ((will be filled in by the editorial staff))

Published online: ((will be filled in by the editorial staff))

Reference

[1] I. You, D. G. Mackanic, N. Matsuhisa, J. Kang, J. Kwon, L. Beker, J. Mun, W. Suh, T. Y. Kim, J. B. H. Tok, Z. N. Bao, U. Jeong, *Science* **2020**, 370, 961.

[2] Q. L. Hua, J. L. Sun, H. T. Liu, R. R. Bao, R. M. Yu, J. Y. Zhai, C. F. Pan, Z. L. Wang, *Nat Commun* **2018**, 9, 244.

[3] D. Jung, C. Lim, H. J. Shim, Y. Kim, C. Park, J. Jung, S. I. Han, S. H. Sunwoo, K. W. Cho, G. D. Cha, D. C. Kim, J. H. Koo, J. H. Kim, T. Hyeon, D. H. Kim, *Science* **2021**, 373, 1022.

[4] Y. Lee, J. Park, A. Choe, S. Cho, J. Kim, H. Ko, *Adv. Funct. Mater.* **2020**, 30, 1904523.

[5] A. Chortos, J. Liu, Z. Bao, *Nat. Mater.* **2016**, 15, 937.

[6] X. L. Ma, C. F. Wang, R. L. Wei, J. Q. He, J. Li, X. H. Liu, F. C. Huang, S. P. Ge, J. Tao, Z. Q. Yuan, P. Chen, D. F. Peng, C. F. Pan, *ACS Nano* **2022**, 16, 2789.

[7] Z. Q. Shen, X. Y. Zhu, C. Majidi, G. Y. Gu, *Adv. Mater.* **2021**, 33, 2102069.

[8] B. B. Ying, R. Z. Chen, R. Z. Zuo, J. Y. Li, X. Y. Liu, *Adv. Funct. Mater.* **2021**, 31, 2104665.

[9] Y. Yu, J. Nassar, C. Xu, J. Min, Y. Yang, A. Dai, R. Doshi, A. Huang, Y. Song, R. Gehlhar, A. D. Ames, W. Gao, *Sci Robot* **2020**, 5, aaz7946.

[10] H. Chen, Y. Jing, J.-H. Lee, D. Liu, J. Kim, S. Chen, K. Huang, X. Shen, Q. B. Zheng, J. Yang, S. Jeon, J.-K. Kim, *Mater. Horiz.* **2020**, 7, 2378.

[11] H. Zhang, D. Liu, J. H. Lee, H. M. Chen, E. Kim, X. Shen, Q. B. Zheng, J. Yang, J. K. Kim, *Nano-Micro Lett* **2021**, 13, 122.

[12] J. H. Lee, H. M. Chen, E. Kim, H. Zhang, K. Wu, H. M. Zhang, X. Shen, Q. B. Zheng, J. Yang, S. Jeon, J. K. Kim, *Mater. Horiz.* **2021**, 8, 1488.

[13] Y. E. Shin, S. D. Sohn, H. Han, Y. Park, H. J. Shin, H. Ko, *Nano Energy* **2020**, 72, 104671.

[14] G. Y. Bae, J. T. Han, G. Lee, S. Lee, S. W. Kim, S. Park, J. Kwon, S. Jung, K. Cho, *Adv. Mater.* **2018**, 30, 1803388.

[15] F. C. Li, Y. Liu, X. L. Shi, H. P. Li, C. H. Wang, Q. Zhang, R. J. Ma, J. J. Liang, *Nano Lett.* **2020**, 20, 6176.

[16] A. Chhetry, S. Sharma, S. C. Barman, H. Yoon, S. Ko, C. Park, S. Yoon, H. Kim, J. Y. Park, *Adv. Funct. Mater.* **2021**, 31, 2007661.

[17] R. Feng, Y. Mu, X. Zeng, W. Jia, Y. Liu, X. Jiang, Q. Gong, Y. Hu, *Sensors* **2021**, 21, 3969.

[18] S. H. Shin, W. Lee, S. M. Kim, M. Lee, J. M. Koo, S. Y. Hwang, D. X. Oh, J. Park, *Chem. Eng. J.* **2019**, 371, 452.

[19] P. C. Zhu, Y. L. Wang, Y. Wang, H. Y. Mao, Q. Zhang, Y. Deng, *Adv Energy Mater* **2020**, 10, 2001945.

[20] Y. Wang, H. T. Wu, L. Xu, H. N. Zhang, Y. Yang, Z. L. Wang, *Sci. Adv.* **2020**, 6, abb9083.

[21] Y. Jung, J. Choi, Y. Yoon, H. Park, J. Lee, S. H. Ko, *Nano Energy* **2022**, 95, 107002.

[22] Y. E. Shin, Y. J. Park, S. K. Ghosh, Y. Lee, J. Park, H. Ko, *Adv. Sci.* **2022**, 9, 2105423.

[23] K. Song, R. Zhao, Z. L. Wang, Y. Yang, *Adv. Mater.* **2019**, 31, e1902831.

[24] M. M. Zhu, M. N. Lou, J. Y. Yu, Z. L. Li, B. Ding, *Nano Energy* **2020**, 78, 105208.

[25] X. D. Wu, M. Ahmed, Y. Khan, M. E. Payne, J. Zhu, C. H. Lu, J. W. Evans, A. C. Arias, *Sci. Adv.* **2020**, 6, aba1062.

[26] J. Park, M. Kim, Y. Lee, H. S. Lee, H. Ko, *Sci. Adv.* **2015**, 1, e150066.

[27] J. X. Xu, C. Y. Ban, F. Xiu, Z. H. Tian, W. J. Jiang, M. J. Zhang, H. S. Zhang, Z. Zhou, J. Q. Liu, W. Huang, *ACS Appl. Mater. Interfaces* **2021**, 13, 30205.

[28] Q. Su, Q. Zou, Y. Li, Y. Z. Chen, S. Y. Teng, J. T. Kelleher, R. Nith, P. Cheng, N. Li, W. Liu, S. L. Dai, Y. D. Liu, A. Mazursky, J. Xu, L. H. Jin, P. Lopes, S. H. Wang, *Sci. Adv.* **2021**, 7, eabi4563.

[29] J. H. Lee, E. Kim, H. Zhang, H. Chen, H. Venkatesan, K. Y. Chan, J. Yang, X. Shen, J. Yang, S. Jeon, J. K. Kim, *Adv. Funct. Mater.* **2022**, 32, 2107570.
[30] Z. Wang, Z. R. Liu, G. R. Zhao, Z. C. Zhang, X. Y. Zhao, X. Y. Wan, Y. L. Zhang, Z. L. Wang, L. L. Li, *ACS Nano* **2022**, 16, 1661.
[31] Y. P. Wang, X. F. Cao, J. Cheng, B. W. Yao, Y. S. Zhao, S. L. Wu, B. Z. Ju, S. F. Zhang, X. M. He, W. B. Niu, *ACS Nano* **2021**, 15, 3509.
[32] Z. Y. Gao, Z. Lou, W. Han, G. Z. Shen, *ACS Appl. Mater. Interfaces* **2020**, 12, 24339.
[33] J. C. Yang, J. O. Kim, J. Oh, S. Y. Kwon, J. Y. Sim, D. W. Kim, H. B. Choi, S. Park, *ACS Appl. Mater. Interfaces* **2019**, 11, 19472.
[34] M. Y. Ma, Z. Zhang, Z. N. Zhao, Q. L. Liao, Z. Kang, F. F. Gao, X. Zhao, Y. Zhang, *Nano Energy* **2019**, 66, 104105.
[35] Y. Wang, W. Zhu, Y. Deng, B. Fu, P. Zhu, Y. Yu, J. Li, J. Guo, *Nano Energy* **2020**, 73, 104773.
[36] X. D. Wu, J. Zhu, J. W. Evans, C. H. Lu, A. C. Arias, *Adv. Funct. Mater.* **2021**, 31, 2010824.
[37] Y. Qiu, Y. Tian, S. S. Sun, J. H. Hu, Y. Y. Wang, Z. Zhang, A. P. Liu, H. Y. Cheng, W. Z. Gao, W. N. Zhang, H. Chai, H. P. Wu, *Nano Energy* **2020**, 78, 105337.
[38] X. D. Wu, J. Zhu, J. W. Evans, A. C. Arias, *Adv. Mater.* **2020**, 32, 2005970.
[39] Q. B. Zheng, J. H. Lee, X. Shen, X. Chen, J. K. Kim, *Mater. Today* **2020**, 36, 158.
[40] X. T. Lai, J. S. Peng, Q. F. Cheng, A. P. Tomsia, G. L. Zhao, L. Liu, G. S. Zou, Y. L. Song, L. Jiang, M. Z. Li, *Angew Chem Int Edit* **2021**, 60, 14307.
[41] G. Kim, S. Cho, K. Chang, W. S. Kim, H. Kang, S. P. Ryu, J. Myoung, J. Park, C. Park, W. Shim, *Adv. Mater.* **2017**, 29, 1606120.
[42] G. J. Chen, W. Hong, *Adv Opt Mater* **2020**, 8, 2000984.
[43] J. Teyssier, S. V. Saenko, D. van der Marel, M. C. Milinkovitch, *Nat Commun* **2015**, 6, 6368.
[44] Y. P. Wang, W. B. Niu, C. Y. Lo, Y. S. Zhao, X. M. He, G. R. Zhang, S. L. Wu, B. Z. Ju, S. F. Zhang, *Adv. Funct. Mater.* **2020**, 30, 2000356.
[45] H. H. Chou, A. Nguyen, A. Chortos, J. W. To, C. Lu, J. Mei, T. Kurosawa, W. G. Bae, J. B. Tok, Z. Bao, *Nat Commun* **2015**, 6, 8011.
[46] Z. Y. Chen, Y. R. Yu, J. H. Guo, L. Y. Sun, Y. J. Zhao, *Adv. Funct. Mater.* **2021**, 31, 2007527.
[47] G. Q. Zu, K. Kanamori, K. Nakanishi, J. Huang, *Chem. Mater.* **2019**, 31, 6276.
[48] Q. Wang, S. J. Ling, X. P. Liang, H. M. Wang, H. J. Lu, Y. Y. Zhang, *Adv. Funct. Mater.* **2019**, 29, 1808695.
[49] J. H. Cai, J. Li, X. D. Chen, M. Wang, *Chem. Eng. J.* **2020**, 393, 124805.
[50] A. Di Bartolomeo, M. Sarno, F. Giubileo, C. Altavilla, L. Iemmo, S. Piano, F. Bobba, M. Longobardi, A. Scarfato, D. Sannino, A. M. Cucolo, P. Ciambelli, *J. Appl. Phys.* **2009**, 105, 064518.
[51] Z. H. Zhang, Z. Y. Chen, Y. Wang, Y. J. Zhao, *PNAS* **2020**, 117, 18310.
[52] X. Shen, Q. B. Zheng, J. K. Kim, *Prog. Mater Sci.* **2021**, 115, 100708.
[53] J. H. Lee, J. Kim, D. Liu, F. Guo, X. Shen, Q. B. Zheng, S. Jeon, J. K. Kim, *Adv. Funct. Mater.* **2019**, 29, 1901623.
[54] S. Yamada, H. Toshiyoshi, *ACS Appl. Mater. Interfaces* **2020**, 12, 36449.
[55] H. S. Guo, M. Bai, Y. N. Zhu, X. M. Liu, S. Tian, Y. Long, Y. M. Ma, C. Y. Wen, Q. S. Li, J. Yang, L. Zhang, *Adv. Funct. Mater.* **2021**, 31, 2106406.
[56] X. Q. Wang, C. F. Wang, Z. F. Zhou, S. Chen, *Adv Opt Mater* **2014**, 2, 652.
[57] Y. H. Ye, Y. F. Zhang, Y. Chen, X. S. Han, F. Jiang, *Adv. Funct. Mater.* **2020**, 30, 2003430.

TOC

A mutually-discriminating trimodal ionic skin is designed to simultaneously detect and decouple in-plane strain, temperature and pressure stimuli by means of multiple sensing principles of the mechanochromic, thermoresistive and triboelectric effects. These three distinct capabilities manifest a highly sensitive response to a selective external stimulus while upholding high insensitivity to extraneous ones.

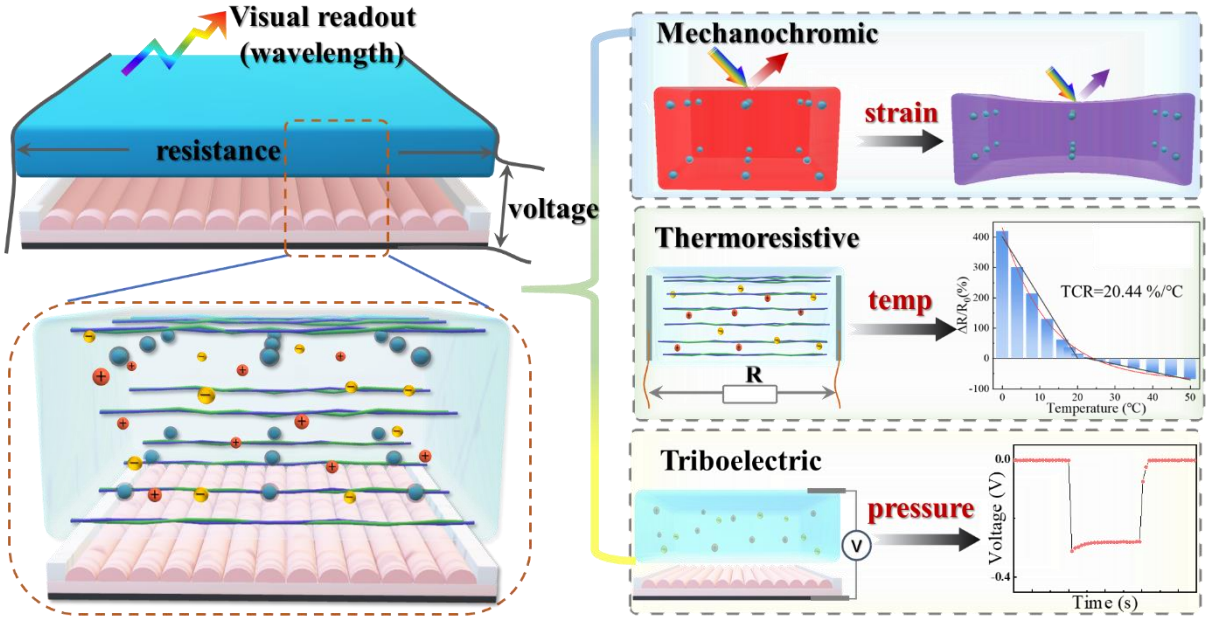

Supporting Information

Bioinspired chromotropic ionic skin with in-plane strain/temperature/pressure multiple sensing and ultrahigh stimuli discriminability

H. Zhang, H. Chen, J.H. Lee, E. Kim, K.Y. Chan[1,3], H. Venkatesan[1], M.H. Adegun[1], O.G. Agbabiaka[1], Prof. X. Shen[1,3*], Prof. Q.B. Zheng, Prof. J.L. Yang[1,5*], Prof. J.K. Kim[1,6*]

[1] Department of Mechanical and Aerospace Engineering, The Hong Kong University of Science and Technology, Clear Water Bay, Kowloon, Hong Kong, China.

[2] Department of Materials Science and Engineering, KAIST Institute for the Nanocentury, Korea Advanced Institute of Science and Technology (KAIST), Daejeon 34141, Korea.

[3] Department of Aeronautical and Aviation Engineering, The Hong Kong Polytechnic University, Hung Hom, Kowloon, Hong Kong, China.

[4] School of Science and Engineering, The Chinese University of Hong Kong, Shenzhen, Guangdong 518172, China.

[5] HKUST Shenzhen-Hong Kong Collaborative Innovation Research Institute, Futian, Shenzhen, China

[6] School of Mechanical and Manufacturing Engineering, University of New South Wales, Sydney, NSW 2052, Australia

E-mail: xi.shen@polyu.edu.hk (X. Shen); maeyang@ust.hk (J.L. Yang); mejkkim@ust.hk (J.K. Kim)

Keywords: ionic skin, multimodal sensing, chromotropic iontronics, hybrid mechanism, stimuli discriminability.

Experimental Section

Materials and synthesis of multi-response chromotropic ionic hydrogels

Ferrocene ($Fe(C_5H_5)_2$, ≥99%), acetone (C_3H_6O, >98%), hydrogen peroxide (H_2O_2, 30%), sodium chloride (NaCl, ≥99%), glutaraldehyde ($C_5H_8O_2$, 50% in water), toluene (C_7H_8, >98%), gelatin (300 g Bloom, Type A, from porcine skin), PVA powder (Mw = 86000 kDa, 99% hydrolyzed) were supplied by Sigma-Aldrich. PDMS (Sylgard 184) was supplied by Dow corning, and both Ecoflex 0030 and silicone adhesive were from Smooth-on. Single-walled CNTs with high purity (≥95%) were supplied by Chengdu Organic Chemical Co. Unless otherwise specified, the materials and chemicals used in this work were used without further purification.

Fe_3O_4@C magnetic particles were synthesized through a hydrothermal reaction.[S1] In a typical

experiment, ferrocene (0.54 g) was dissolved in acetone (54 mL) under ultrasonication for 5 min and mechanical stirring for 20 min. Subsequently, hydrogen peroxide was added dropwisely to the solution which was vigorously stirred for another 30 min. The amount of hydrogen peroxide (1.1-2.0 mL) determined the size of synthesized nanoparticles ranging 130-250 nm. The obtained solution was sealed in a polyphenylene-lined stainless-steel autoclave (100 mL) at 230 ℃ for 70 h. After the reaction, the resulting products were separated by a magnet and washed several times with acetone. Finally, the Fe_3O_4@C particles were dried in a vacuum oven at 40 ℃.

Mechanochromic ionic hydrogels were prepared by assembling Fe_3O_4@C in the gelatin/PVA matrix using a magnetic field-assisted directional freezing method. First, a 10% (w/v) gelation solution was prepared by dissolving gelatin powders in deionized (DI) water at 80 ℃ for 30 min. The Fe_3O_4@C powders were then added to the gelation solution, followed by stirring and sonication at 60 ℃ for 15 min. The PVA powders were subsequently added to DI water and stirred at 90 ℃ for 2 h to obtain a fully dissolved 10% (w/v) PVA solution. Then, an appropriate amount of the PVA solution was mixed with the Fe_3O_4@C-gelatin mixture solution under vigorous stirring. Different gelatin to PVA mass ratios of 100:0, 90:10, 75:25, 60:40 and 50:50 were used while the total polymer content was fixed at 10%. NaCl powders were dissolved to control the ion concentration ranging from 0 to 0.5 M. Glutaraldehyde (2 ml 0.5% solution) chemical crosslinking agent was added to the prepolymer solution to avoid the phase separation between PVA and gelatin monomers, which was thoroughly mixed by mechanical stirring for 30 min. After complete degassing in the sonicator, the homogeneous solution was poured into the 3D printed mold (of volume 20 mm × 20 mm × 1 mm). Next, the mold was quickly placed on top of a copper billet, half of which was submerged in the liquid nitrogen. At the same time, a cuboid magnet (of size 50 mm × 50 mm × 20 mm) was placed at the side of the mold to build an external magnetic field for the Fe_3O_4@C nanoparticles. After the solution was completely frozen, the mold was placed in a refrigerator at -20 ℃ overnight and kept at 4 ℃ for 12 h to

ensure the completion of physicochemical polymerization. Finally, the prepared hydrogel films were immersed in the water/ethylene glycol (1:1) solution for 2 h to neutralize the GA and finish the solvent displacement process.

Preparation of wrinkle-patterned, flexible PDMS electrodes with modulated moduli

The wrinkle-patterned microstructures with modulated moduli were fabricated via a solution casting method. Firstly, the modulus of PDMS was controlled by varying the concentration ratio of the base to curing agent. The hard PDMS prepolymer with a base to curing agent weight ratio of 2:1 was cast onto a template with inverse wrinkle patterns (as described in Figure S10). The excess prepolymer was carefully removed with a spatula to ensure that the polymer only filled the grooves. The hard PDMS block with semi-cylindrical patterns was cured at 60 °C for 2 hr. The soft PDMS layer of thickness 20 μm was prepared using a base to curing agent weight ratio of 20:1, which was spin-coated at 800 rpm for 1 min on the surface of hard PDMS and cured similarly. The flexible PDMS assembly consisting of a wrinkle-patterned hard layer and a soft substrate functioned as the friction layer in the triboelectric structure.

The CNT-based electrode was prepared by coating the CNT/soft PDMS composite on the friction layer. 0.5 g CNTs were added to 20 ml volatile toluene solvent and ultrasonicated for 2 h to ensure complete dispersion. PDMS base monomer of 5 g was added to the CNT dispersion and stirred thoroughly to evaporate the volatile organic solvent. Then, 0.25 g curing agent (at a base to curing agent ratio of 20:1) was added and thoroughly mixed, which was coated on the soft substrate at a thickness of ~150 μm and cured similarly.

Integration of chromotropic ionic skin and sensor array

The chromotropic ionic skin system was fabricated by integrating the ionic hydrogel layer, wrinkle-patterned friction layer and a CNT/PDMS elastic electrode. The ionic hydrogel film was cut into a 10 mm × 10 mm square and connected to carbon conductive tapes at both ends. After peeling off the fabricated winkle-patterned friction layer and elastic electrode, two spacers (Ecoflex, part A: part B=1:1) of 10 mm × 3 mm × 0.5 mm in dimensions were adhered to two

ends of the hydrogel film and attached to the winkle pattern using silicone adhesive. Another carbon conductive tape was attached to the bottom CNT/PDMS electrode. Finally, the entire ionic skin was encapsulated with Ecoflex by spin coating at 1000 rpm for 30 s. For fabrication of the large-area sensor array of 16 units, the same procedure was employed several times at different regions to form square-shaped sensor arrays of 42 mm × 42 mm square. The gaps between different units were filled with Ecoflex.

Characterization of ionic skin and measurements of sensor performance

The SEM (JSM-7100) and TEM (JEOL 2010) were used to examine the morphologies of the Fe_3O_4@C magnetic nanoparticles. The anisotropic structure prepared by the directional freezing was characterized by a freeze-drying method. The frozen ionic hydrogel was freeze-dried in a freeze drier (SCIENTZ-10 N) at -50 ℃ for 5 days to prepare samples for the SEM analysis of aligned polymer chains and ordered magnetic nanoparticles. The morphology of photonic crystals was revealed by examining the cross-sectional cut of the chromotropic film. The chemical composition of gelatin was measured by the Fourier transform infrared spectroscopy (FT-IR, Bruker Vertex 70 Hyperion 1000). The ZetaPlus was used to measure the zeta potential of the magnetic nanoparticle suspension to indicate the degree of dispersion. The universal testing machine (UTM-12) equipped with digital multimeters was used to measure the mechanical properties of ionic hydrogels and PDMS films, including tensile, compression and stretching/releasing cyclic properties. The strain-stress curves were recorded by stretching or compressing the samples at a strain rate of 15 mm/min at room temperature (23 ℃). To perform the bending test, the chromotropic film was attached to two fixtures at both ends. One fixture remained stationary, while the other was connected to a linear motor to apply different bending strains by adjusting the distance between the two ends, as shown in Figure S7. The temperature sensing performance of the E-skin was evaluated by placing it on the ice or a hot plate to obtain a temperature variation from 0 to 50 ℃. The electrical resistance and voltage signals at different tensile or compressive strains were detected by a digital multimeter (34970A

Data Acquisition, Agilent) by connecting the ends of the hydrogel and CNT/PDMS electrode using a conductive carbon tape. The reflection spectra of different structural colors were acquired by optical microscopy with a fiber-optic spectrometer (USB2000, Ocean Optics) at a fixed glancing angle. The temperatures of different samples were recorded using a UT320 thermometer. The ionic conductivities of hydrogels were characterized by electrochemical impedance spectroscopy (EIS) on an electrochemical workstation. All the reported electrical and optical measurements were the average values obtained from at least three tests. The cyclic tensile tests were carried out between 0 and 110% strains for 20 cycles at room temperature. The long-term temperature sensing stability was measured by monitoring the resistance in response to temperature changes between 10 and 40 ℃ for 200 cycles. The cyclic compression tests of the e-skin were performed by applying and removing a pressure of 1 kPa for 1000 cycles. The stress distribution on the concave surface of the bent chromotropic ionic hydrogel films, volumetric strain and deformation of the wrinkle-patterned friction layer with and without gradient moduli were numerically calculated using the commercial finite element software, Comsol. The parameter settings, including the size of models, mechanical properties and boundary conditions of mechanical loading, were determined by experimental data of the ionic hydrogel film, hard PDMS, soft PDMS and CNT/PDMS layers.

Supplementary Figure Clips

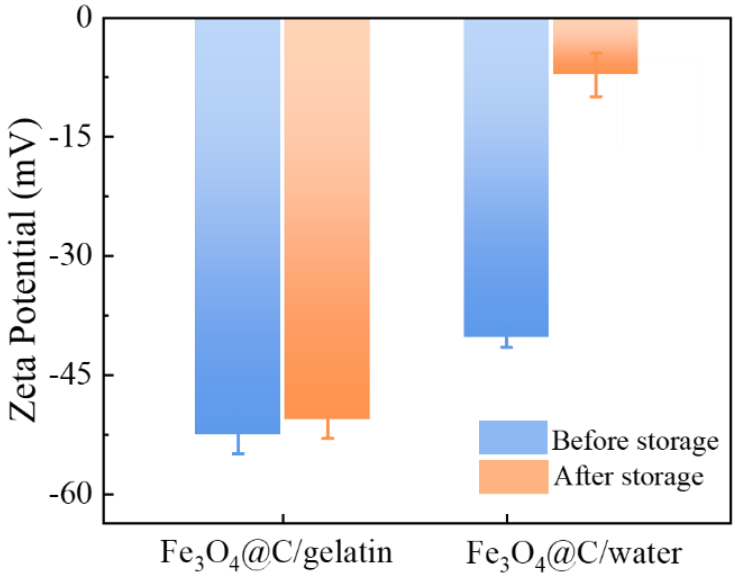

Figure S1. Zeta potentials of Fe_3O_4@C magnetic nanoparticles dispersed in gelatin solution (Fe_3O_4@C/gelatin) and deionized water (Fe_3O_4@C/water) measured before and after 2 hr of storage. The dispersions are subjected to an external magnetic field.

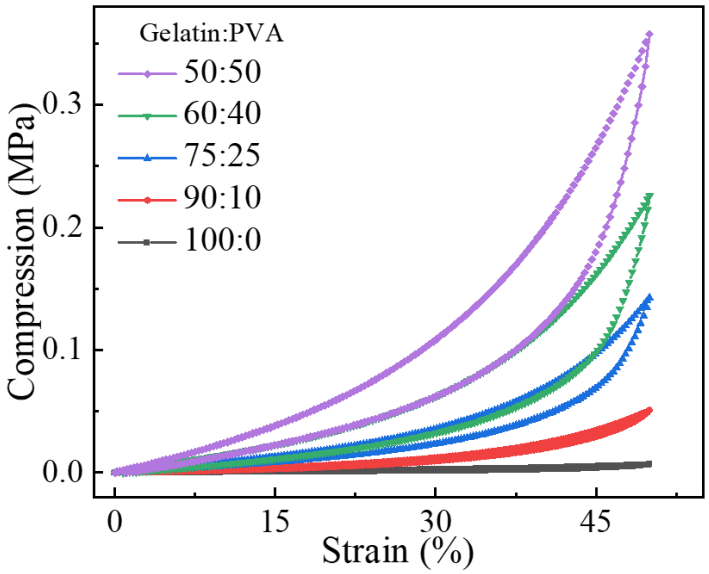

Figure S2. Compressive stress-strain curves of the gelatin/PVA blends with gelatin to PVA weight ratios ranging from 100:0 to 50:50.

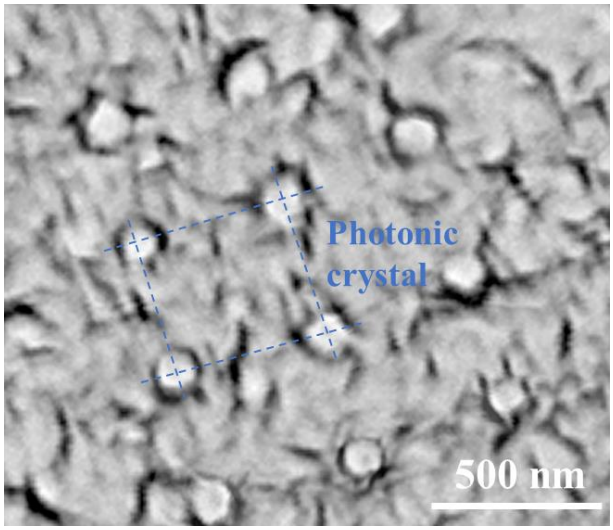

Figure S3. SEM image of the photonic crystal Fe_3O_4@C particle array embedded in the ionic hydrogel.

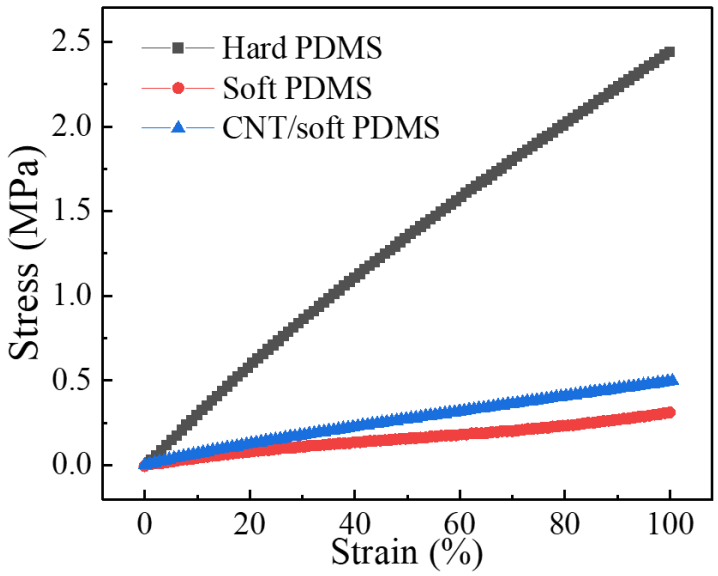

Figure S4. Tensile stress-strain curves of the hard PDMS (2:1), soft PDMS (20:1) and CNT/soft PDMS (20:1) composite.

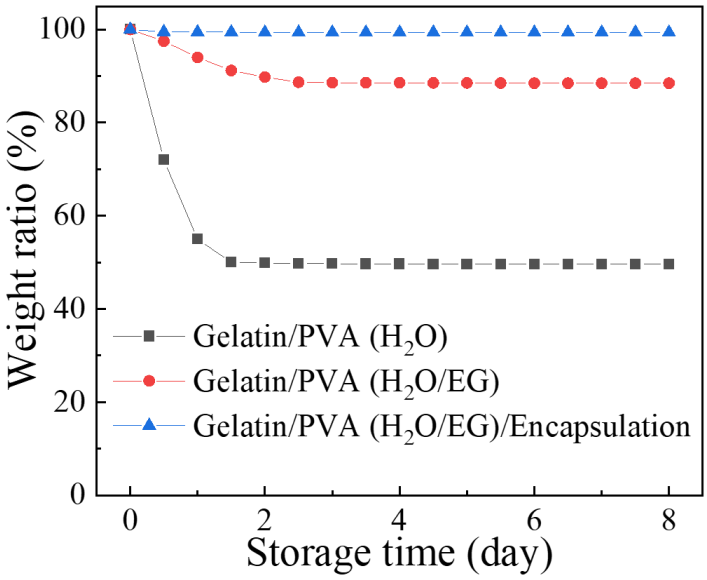

Figure S5. Weight changes of gelatin/PVA hydrogel with water solvent, gelatin/PVA with water/EG solvent and gelatin/PVA with water/EG solvent and Ecoflex encapsulation as a function of time at room temperature. The encapsulated gelatin/PVA hydrogel with water/EG solvent showed no weight reduction even after 8 days, in contrast to the significant weight losses for those without encapsulation and with water as the solvent."

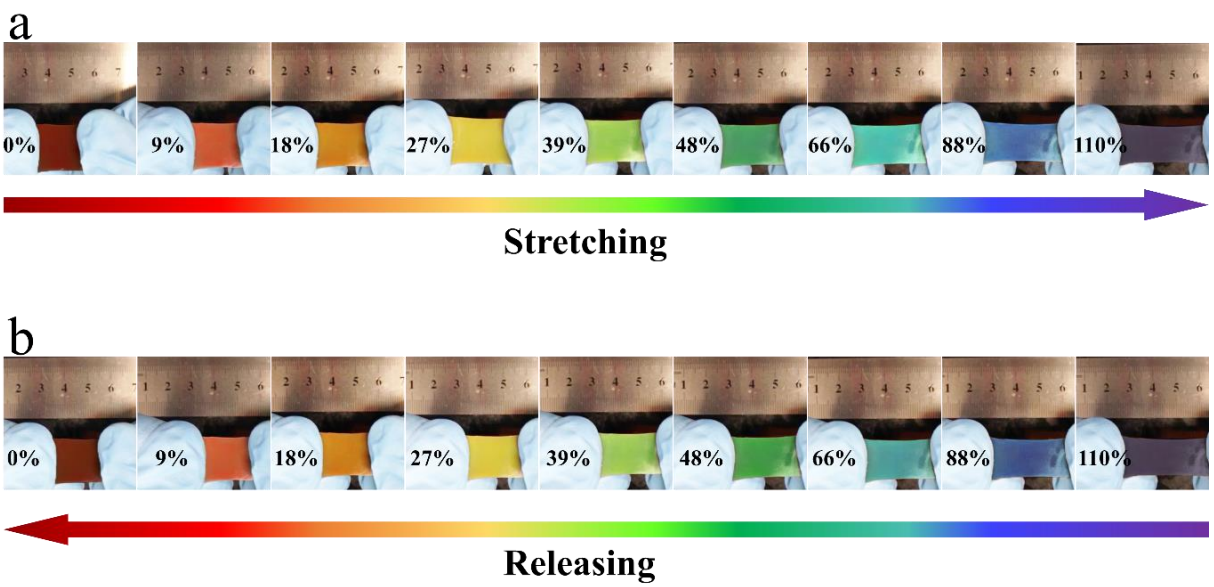

Figure S6. Series of photographs of the chromotropic strain sensor with initial dark red color taken at different strains during a (a) stretching and (b) releasing cycle.

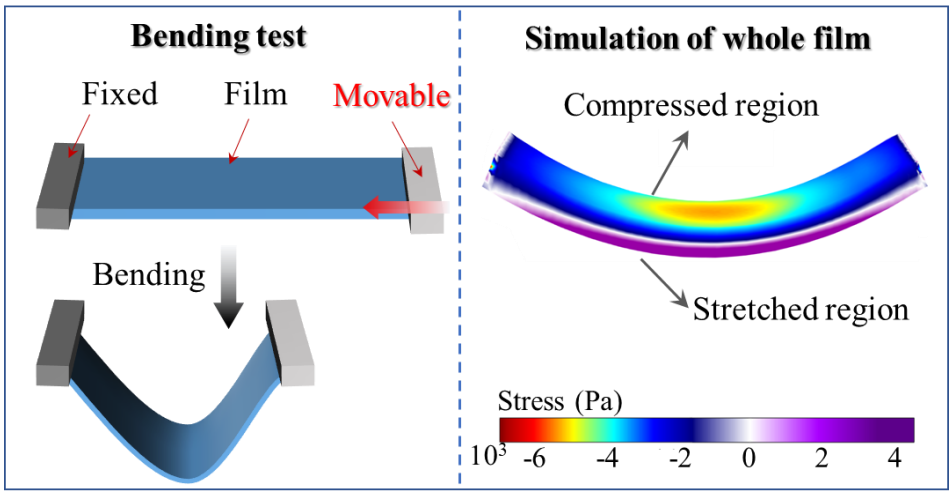

Figure S7. Schematic of the bending test setup and simulated stress distribution of the bent film with a compressed region on its concave surface and a stretched region on the convex surface.

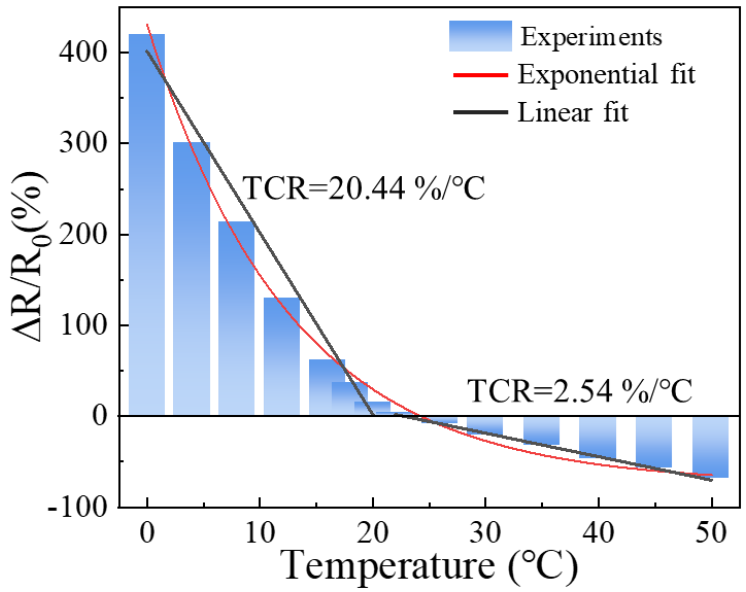

Figure S8. Relative resistance changes measured at different temperatures and their exponential curve and two segmented linear fits.

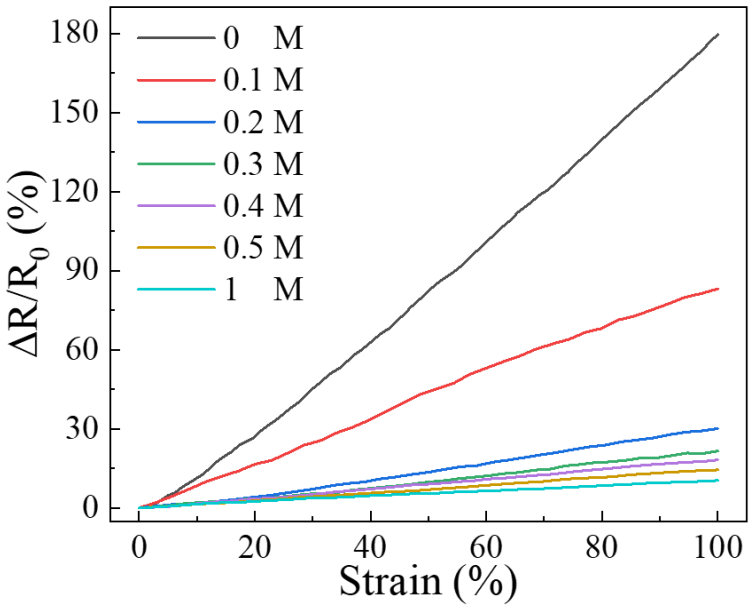

Figure S9. Relative resistance changes versus tensile strain of the ionic films with different NaCl concentrations ranging from 0 to 1M.

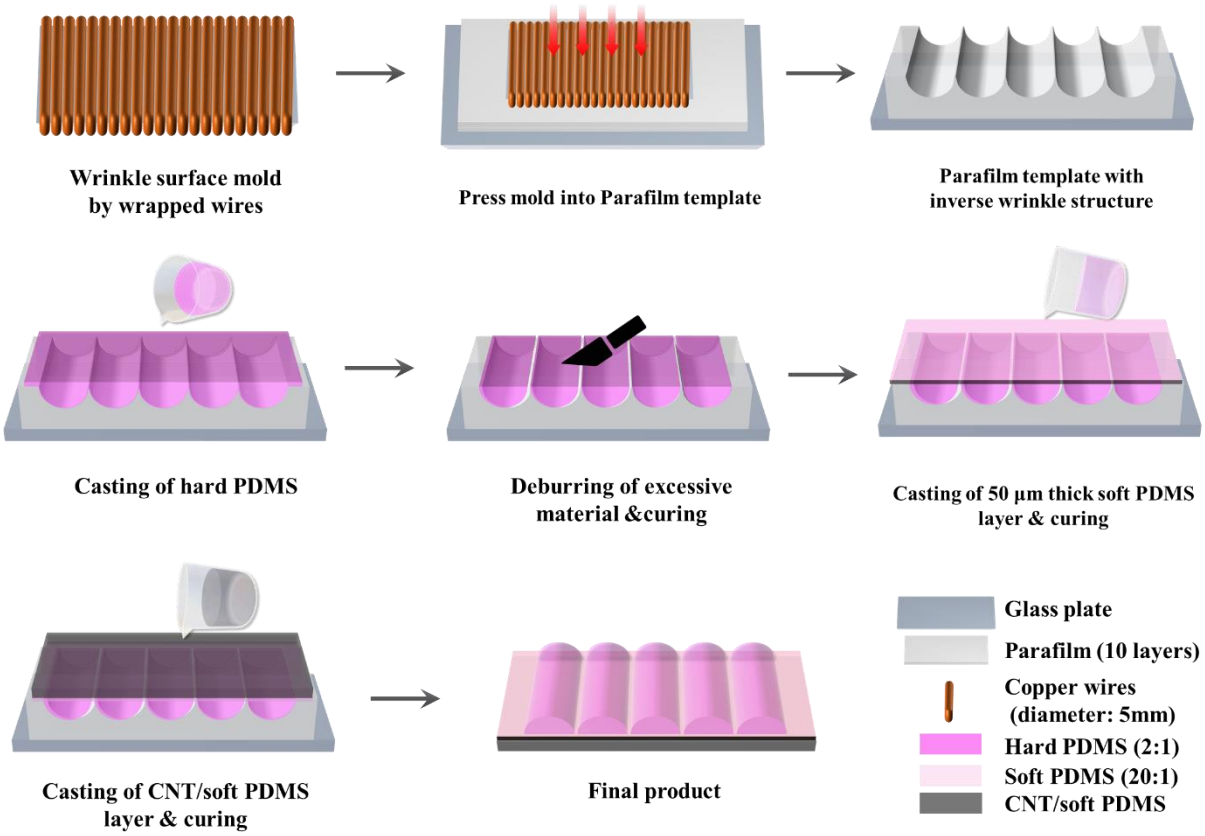

Figure S10. Preparation of the wrinkle-patterned PDMS friction layer with a gradient modulus structure and the CNT-based elastic electrode. First, copper wires with a diameter of 0.5 mm are tightly wrapped around a steel plate and pressed into a ceraceous template (made by stacking

10 layers of Parafilm on a glass plate) under ~2 MPa for 10 min at ambient temperature. Subsequently, the template is stored at -20 °C in a refrigerator for 2 hr, followed by removal of wires from the template. An inverse wrinkle-patterned template is obtained.

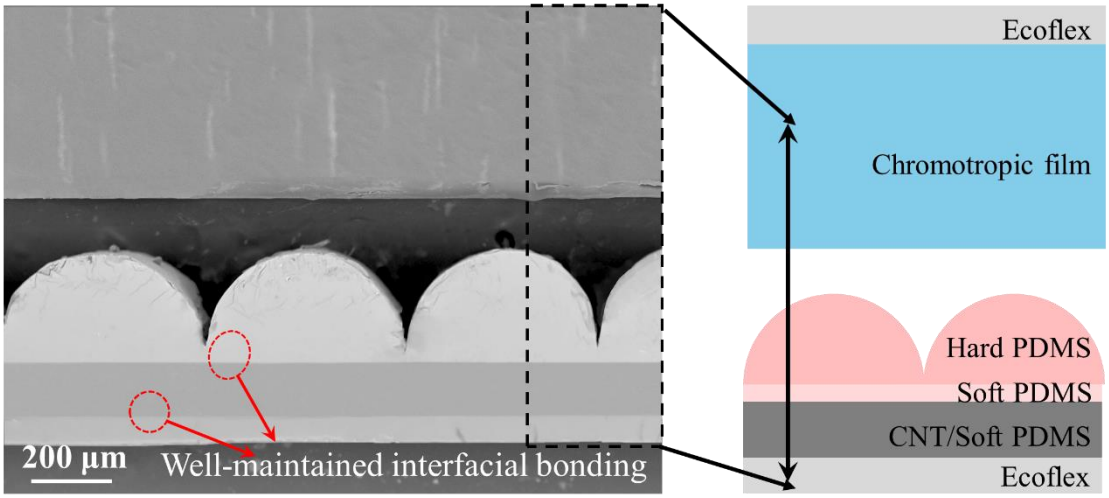

Figure S11. Cross-sectional SEM image showing well-maintained interfaces among multilayers in the e-skin after 1000 stretching/releasing cycles. The right panel illustrates the multilayer configuration of the e-skin.

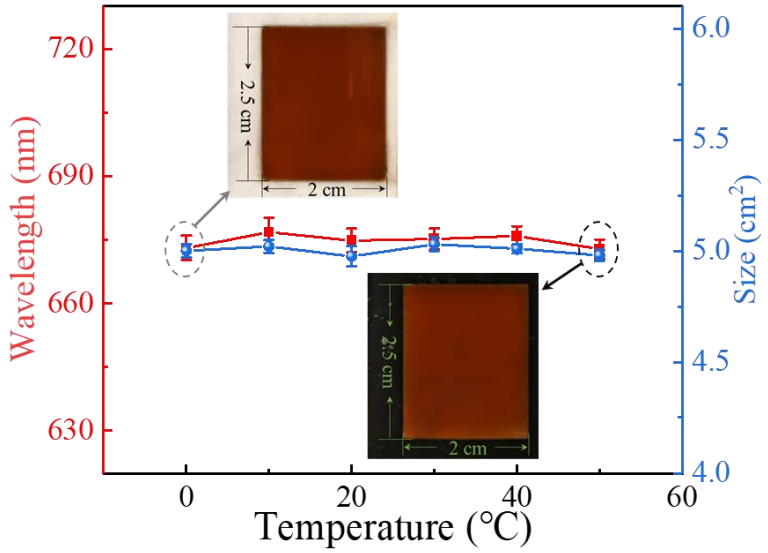

Figure S12. Chromotropic ionic film with initially dark red structural color showing no color change and excellent dimensional stability in response to temperature variation.

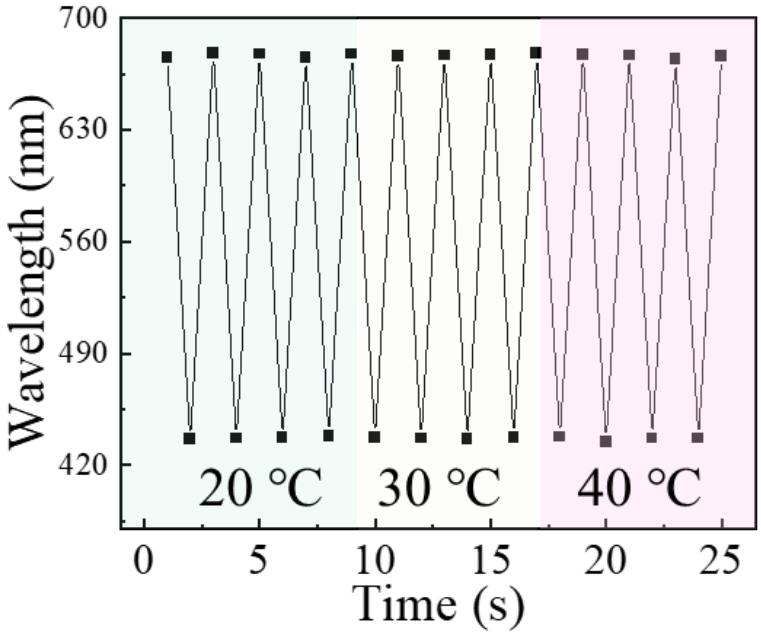

Figure S13. Reflectance wavelength of the ionic skin in response to stretching/releasing cycles at different temperatures.

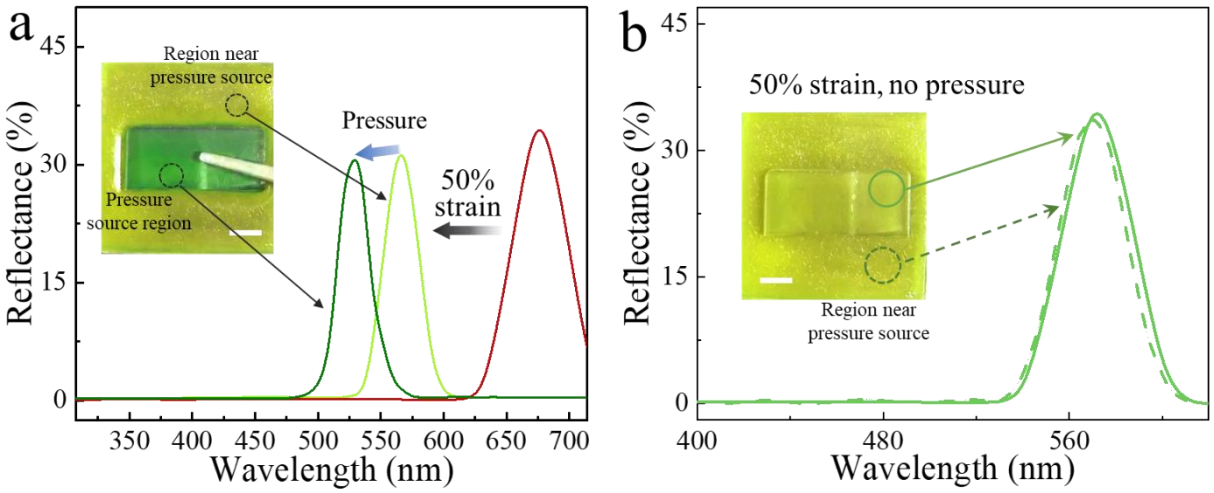

Figure S14. (a) Reflectance spectra of the initial dark red film under a combination of 50% in-plane strain and a pressure of 500 Pa recorded by detecting the structural color at the pressure source and the region surrounding it; and (b) reflectance spectra of the film under 50% in-plane strain and no pressure, indicating accurate in-plane strain response shown in the same region, scale bar = 10 mm.

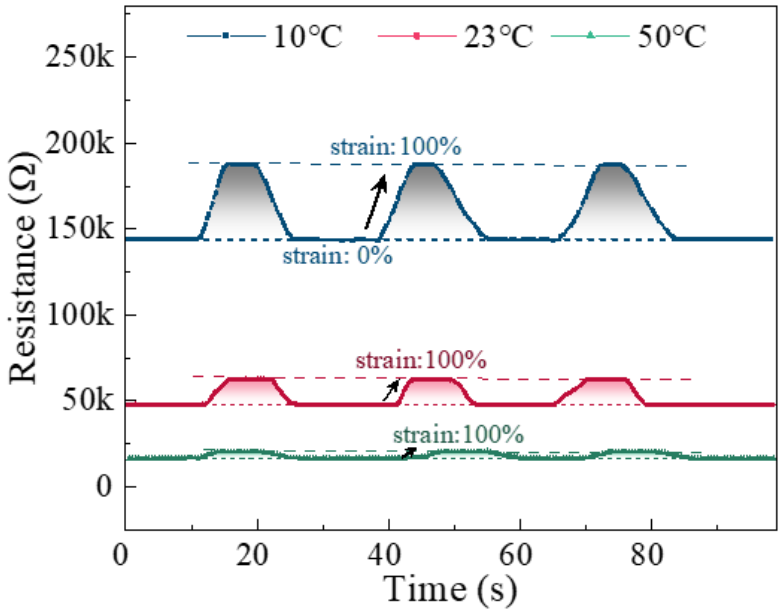

Figure S15. Resistance changes of the ionic hydrogel film when stretched to 100% strain at different temperatures, 10, 23, and 50 °C.

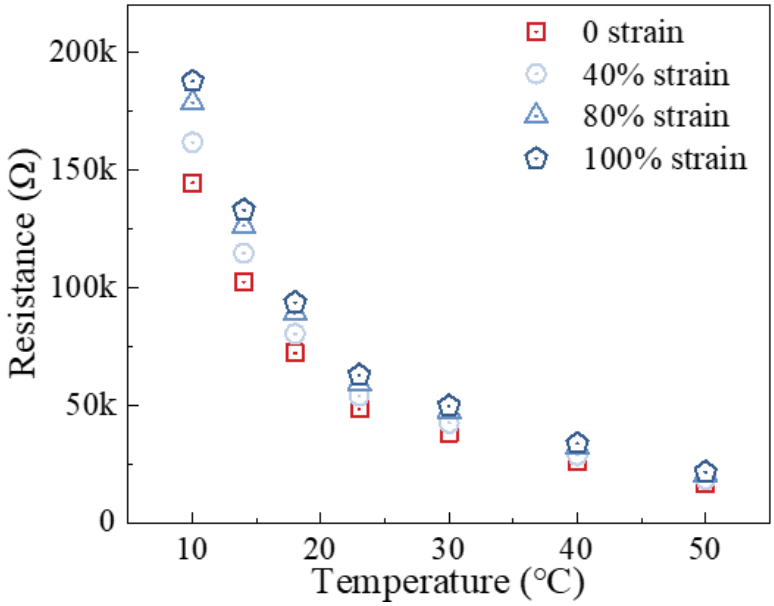

Figure S16. Resistance variation of the ionic skin when stretched to different strains at different temperatures ranging from 10 to 50 °C.

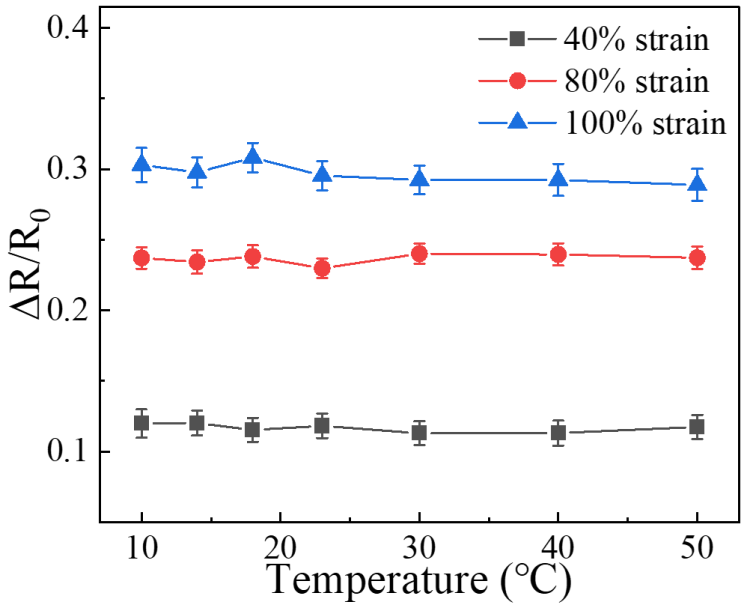

Figure S17. Relative resistance changes of the ionic skin when stretched to different strains at different temperatures.

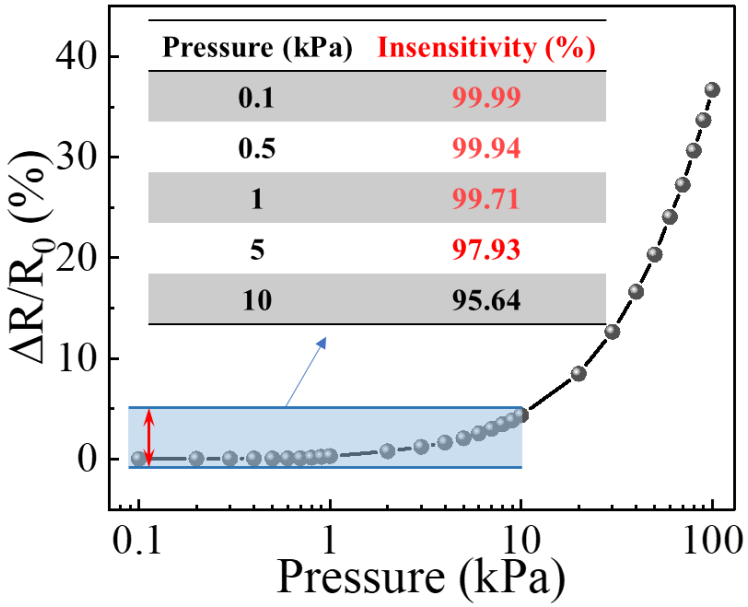

Figure S18. Relative resistance changes and calculated pressure-insensitivity at different pressures ranging from 0 to 100 kPa. The insensitivity (η) is defined as η=1-$\Delta R/R_0$ where $\Delta R/R_0$ is the relative resistance change measured at different pressures.

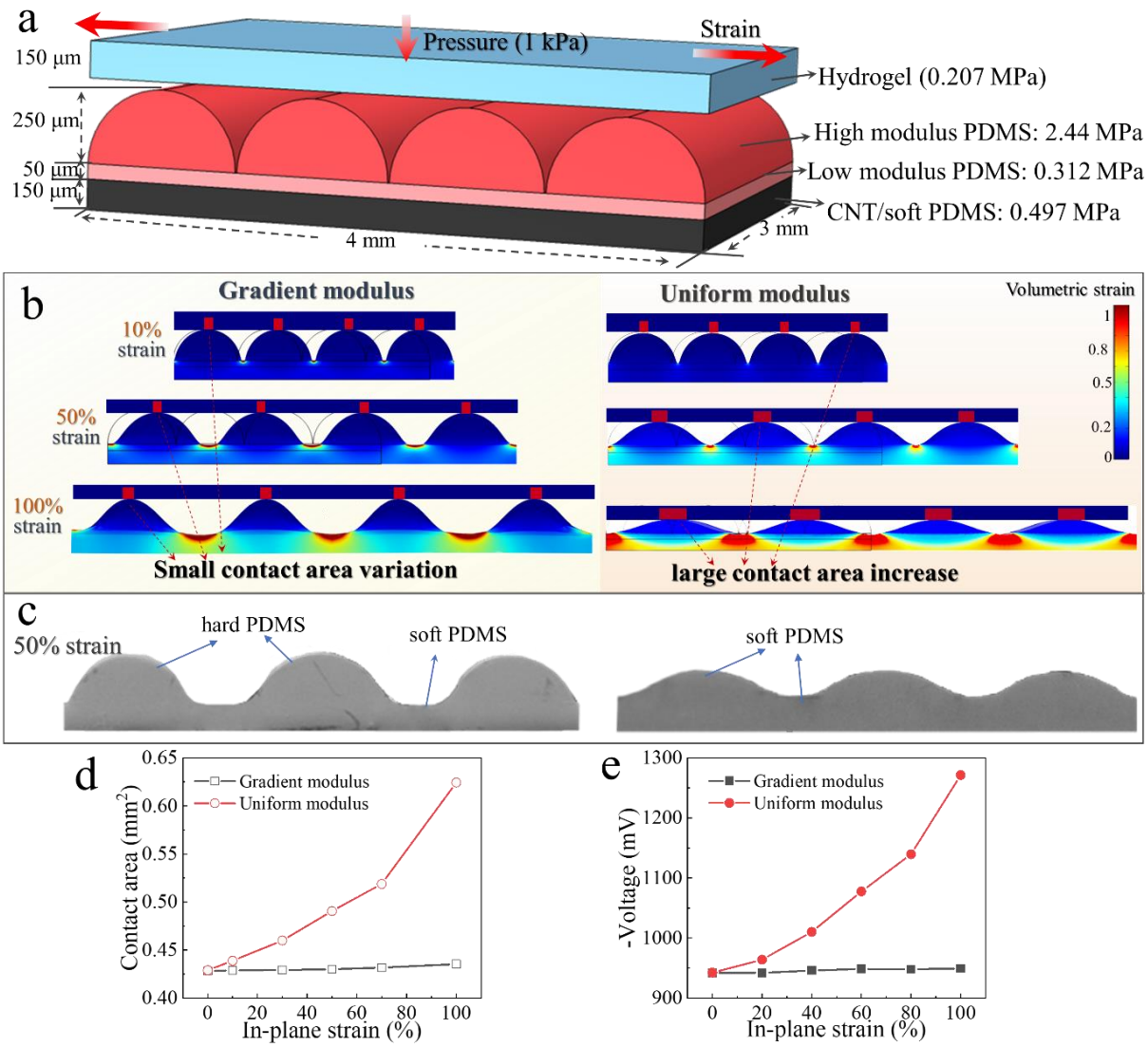

Figure S19. (a) Model with a gradient modulus structure used for Comsol numerical simulations. (b) Comparison of the changes in contact area and volumetric strain distribution between the models having gradient modulus and uniform modulus structures under a constant pressure (1 kPa) and different in-plane strains (10%, 50% and 100%). (c) Cross-sectional SEM images of two different models. (d) Contact area and (e) voltage (in negative sense) vs in-plane strain in two different models, showing insensitivity of the pressure sensor with a gradient modulus structure to in-plane strain stimulus.

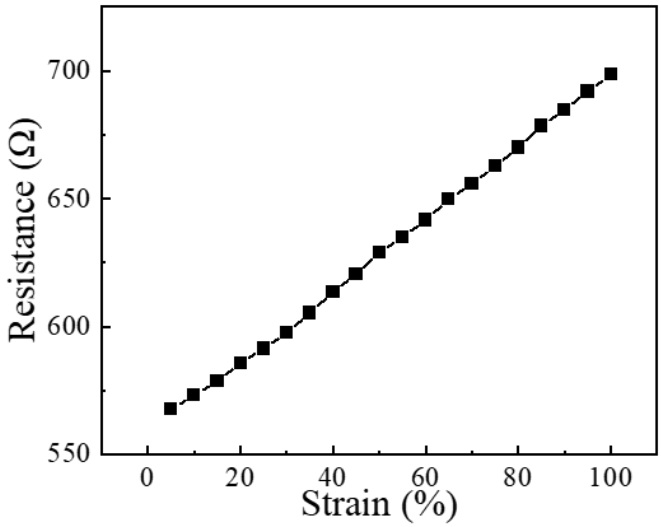

Figure S20. Resistance versus in-plane strain of the stretchable CNT/PDMS electrode.

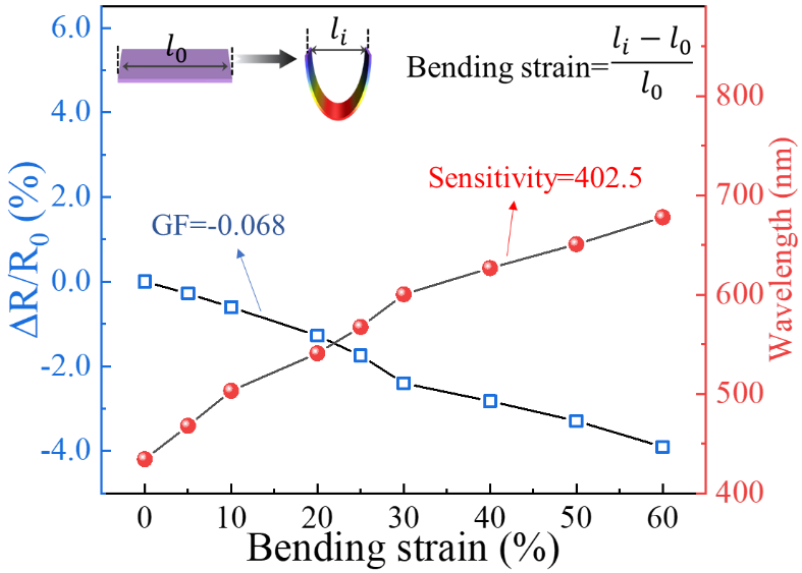

Figure S21. Relative resistance changes and reflectance wavelength of the ionic hydrogel film when subjected to bending (X-axis in negative sense). The inset equation is used for the calculation of bending strain on the concave side.[S2, S3]

Relationship between the reflective wavelength of structural color, applied tensile strain and pressure.

When the chromotropic hydrogel film is stretched along the longitudinal direction at a strain of ε_x, its thickness is reduced according to the Poisson effect.[S1, S4] The strain generated thereby in the thickness direction is defined as ε_z and can be expressed in terms of the Poisson's ratio (ν): $\varepsilon_z = -\nu\varepsilon_x$. Combining the Bragg's equation of photonic crystals, the center-to-center distance between the adjacent magnetic nanoparticles located along the thickness direction of the mechanochromic hydrogel film decreases from the initial, d_0, to the reduced, d_1, upon extension, according to the following equation:[S5]

$$\frac{d_1 - d_0}{d_0} = -\nu\varepsilon_x \quad (1)$$

$$d_1 = d_0(1 - \nu\varepsilon_x) \quad (2)$$

The reduced interparticle distance means a reduced refractive wavelength of the structural color given by the following equation:

$$\lambda max = 2d_1 n_{average} \quad (3)$$

$$= 2d_0(1 - \nu\varepsilon_x)n_{average} \quad (4)$$

where λ_{max} is the wavelength of the reflection peak and $n_{average}$ is the average refractive index of the gelatin/PVA polymer.

Conversely, when the extrusion force is applied to the chromotropic film, the strain along the longitudinal direction, ε_x, contributes to an increase in its thickness, $\nu\varepsilon_x$. The enlarged interparticle distance led to an increase in the reflective wavelength and red-shift of the structural color, which can be expressed by the following equation:

$$\lambda max = 2d_0(1 + \nu\varepsilon_x)n_{average} \quad (5)$$

Resistance-temperature function of thermoresistive ionic hydrogel

The electrical conductivity of chromotropic ionic hydrogels originates from the migration of free ions (Na^+, Cl^-). As the temperature increases, the diffusion rate of free ions also accelerates,

which can be explained by the Arrhenius law:

$$R = Ae^{\frac{-Q}{2k_BT}} + C \quad (6)$$

where R is the rate constant, Q is the thermal activation energy, k_B is the Boltzmann constant, T is the absolute temperature, and A and C are the fitting coefficients. The exponential temperature-dependent resistance implies an ultrahigh variation from low to high temperatures, and the fitted resistance against temperature is given by:

$$R = 215358e^{(-T/12.66)} + 10899.65 \quad (7)$$

Additionally, the relative resistance change can also be described by the exponential function, as shown in Figure S8.

$$\frac{\Delta R}{R_0} = 504.94e^{(-T/12.66)} - 74.44 \quad (8)$$

Here, the initial resistance, R_0, is taken at 23 °C.

Decoupling temperature information from the strain/temperature multiple stimuli

To realize the stimuli discriminability of the ionic hydrogel temperature sensor, the interference between the temperature and strain responses can be modulated by developing the following signal separation procedure given the ultrahigh temperature sensitivity and extremely low strain sensitivity.

When the temperature sensor is subjected to simultaneous temperature and in-plane strain stimuli, the resistance signals detected by the LCR meter (R_{test}) come from two components: one is the resistance produced by the temperature stimulus without strain, R_{temp}; and the other is the additional resistance due to in-plane strain, R_{strain}. Thus,

$$R_{test} = R_{temp} + R_{strain} \quad (9)$$

Here, R_{temp} is equal to the resistance measured by the single-mode temperature sensor. For temperature sensing, R_{strain} is extraneous and can be regarded as the measurement error. It is found that the relative resistance (R_{strain}/R_{temp}) is consistently ≈30% when the sensor is stretched to 100% strain at all temperatures applied (Figure S17). Interestingly, the same

observation with a consistent relative resistance value is noted when the sensor is subjected to another in-plane strain. Based on this finding, R_{temp} for strains is derived:

$$\frac{\Delta R}{R_0} = \frac{\mathrm{R_{strain}}}{\mathrm{R_{temp}}} = \frac{\mathrm{R_{test}} - \mathrm{R_{temp}}}{\mathrm{R_{temp}}}$$

$$\mathrm{R_{temp}} = \frac{\mathrm{R_{test}}}{1 + \frac{\Delta R}{R_0}} \quad (10)$$

Given the almost perfectly linear relationship between the relative resistance change, $\Delta R/R_0$, and the applied strain, ε (Figure S9), Equation S10 for the ionic film with an optimal NaCl concentration of 0.2 M, as a special case, can be written as:

$$\mathrm{R_{temp}} = \frac{\mathrm{R_{test}}}{1 + 0.3\,\varepsilon} \quad (11)$$

Here, $\Delta R/R_0 \approx 0.3\,\varepsilon$ is taken from Figure S17 for the ionic film with a constant NaCl concentration of 0.2M at all temperatures. Therefore, the resistance signal from the mixed stimuli is now modulated using Equation S10 or S11 to obtain the accurate resistance value arising from the temperature stimulus acting alone, R_{temp}. The results for 100% strain are summarized in Table S2 where it is note that the signal error for temperature sensing is now reduced to 0.2%, equivalent to an ultrahigh strain insensitive of 99.8%. Similarly, ultrahigh insensitivities of 99.6% and 99.7% are obtained after modulation when the temperature sensor is subjected to simultaneous extraneous strains of 40 and 80%, respectively.

Furthermore, the chromotropic ionic skin is likely be subjected to stimulation of strain, temperature and pressure acting simultaneously in real application of sensors. The applied in-plane strain, ε, is likely an unknown parameter. To measure ε, it is necessary to use the temperature-insensitive structural color of the photonic crystal structure. The linear relationship between the reflective wavelength, λ_{max}, and the applied strain, ε, presents a slope of -230, which is defined as the strain sensitivity based on wavelength signals, as shown in Figure 3g. The linear relationship gives:

$$\lambda_{max} = -230 \times \varepsilon + 666.8 \quad (12)$$

$$\varepsilon = -0.0043 \times \lambda_{max} + 2.90 \quad (13)$$

Combining Equations S11 and S13, R_{temp} is given by:

$$R_{temp} = \frac{R_{test}}{1.87 - 0.0013 \times \lambda_{max}} \quad (14)$$

where λ_{max} is the detected wavelength spectrum of the structural color. Both R_{test} and λ_{max} are measurable to calculate R_{temp}.

The reflectance wavelength of the structural color gradually increased from initial violet (434 nm) to dark red color (678 nm) with increasing bending strain (in negative sense), as shown in Figure S21. However, the color changing behavior of the bent film was rather uneven (Figure 6h <iii>), thus the maximum reflectance wavelength was used to decouple the temperature information from the strain stimulus. The calculated sensitivities for bending strains based on the resistance and wavelength signals are -0.068 and 402.5 respectively, and the formulas corresponding to these curves are given respectively by:

$$\frac{\Delta R_{bend}}{R_0} = \frac{\Delta R_{strain}}{R_0} = -0.068\ \varepsilon \quad (15)$$

$$\lambda_{max} = 402.5\ \varepsilon + 455.9 \quad (16)$$

where ΔR_{bend} is the resistance change due to bending strain acting alone. The resistance signal detected by the LCR meter (R_{test}) under the simultaneous temperature and bending strain stimuli can be expressed by:

$$\mathrm{R_{test}} = \mathrm{R_{temp}} - \mathrm{R_{bend}} \quad (17)$$

Therefore, combining Equations S11, S16 and S17 gives:

$$R_{temp} = \frac{R_{test}}{1 - 0.068\ \varepsilon} = \frac{R_{test}}{1.077 - 0.00017\ \lambda_{max}} \quad (18)$$

After decoupling temperature resistance from the simultaneous strain/temperature/pressure stimuli using Equation S18, a 3D map of temperature distribution is constructed in the built sensory array, as shown in Figure 6i <ii>.

Table S1. Compositions and molecular structures of different functional layers in the e-skin.

E-skin	Multilayers		Content	Molecular structure
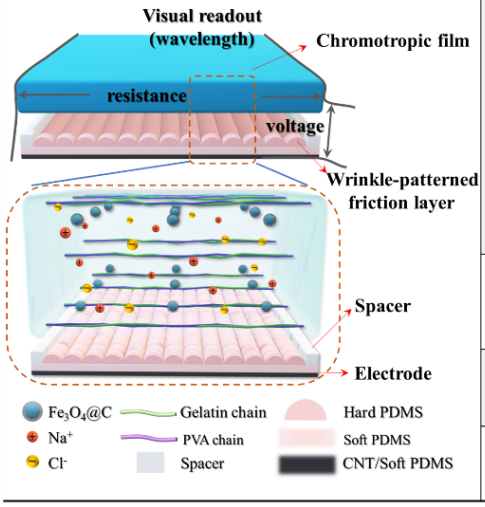	chromotropic film	Polymer (10%)	Gelatin: 50%	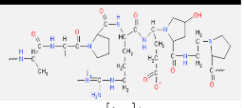
			PVA: 50%	
		Crosslinking agent	Glutaraldehyde: 2 mL 0.5%	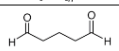
		Ions	NaCl: 0.2 M	-
		Solvent	ethylene glycol: 50% water: 50%	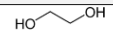 -
	Wrinkle patterned friction layer	Hard PDMS	Base : curing agent = 10:1	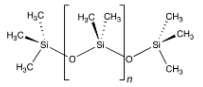
		Soft PDMS	Base : curing agent = 20:1	
	Electrode	CNT/soft PDMS	CNT: 10%	
			Base : curing agent = 20:1	-
	Spacer and encapsulation layer	Ecoflex	Ecoflex	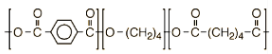

Table S2. Resistance values, R_{temp} and R_{test}, of the ionic hydrogel film measured at 0 and 100% strains under different temperatures and the resistance values after modulation, R_{temp}, showing strain-insensitivity performance based on Equation S11.

Temp. (℃)	0% strain, R_{temp} (Ω)	100% strain					
		R_{tested} (Ω)	R_{strain} (Ω)	Error (%)	Modulated R_{temp} (Ω)	Modulation error (%)	Strain insensitivity (%)
10	144238	187156	42918	29.8	143966	0.188	**99.8**
14	102194	133056	30862	30.2	102351	0.154	**99.9**
18	71971	93631	21659	30.1	72024	0.073	**99.9**
23	48160	62754	14594	30.3	48272	0.233	**99.8**
30	38101	49648	11547	30.3	38191	0.236	**99.8**
40	25843	33429	7786	29.4	25715	0.495	**99.5**
50	16504	21455	5051	30.0	16504	0.003	**100.0**
						Average	**99.8**

Table S3. Voltage values recorded at 0 and 80% strains under different pressures.

Pressure (Pa)	0% strain	80% strain	Voltage variations, ΔV (mV)	Relative voltage variations, $\Delta V/V_0$ (%)
200	-354.0	-363.5	9.5	**2.67**
400	-574.2	-585.9	11.7	**2.04**
600	-707.4	-717.4	10.0	**1.41**
800	-815.3	-834.1	18.8	**2.31**
1000	-927.6	-954.8	27.2	**2.93**
1200	-1034.6	-1051.6	17.0	**1.65**
1400	-1122.2	-1138.0	15.8	**1.41**
1600	-1198.8	-1211.3	12.5	**1.04**

Table S4. Comparison of sensing performance between our trimodal e-skin and existing state-of-the-art multimodal sensors.

	Stimuli	Signal	Material	Mechanism	Sensitivity	Discriminability	Ref.
Bimodal	Temperature / strain	Charge relaxation time; capacitance	Solid state ion conductor	Ion relaxation	Temperature: 12.4%/℃ Strain: 10.4%	Yes (99.4%)	(1)
	Pressure/ Temperature	Capacitance; Resistance	RGO/Al_2O_3, SiO_2, Perylene/SWNT-PDMS	Capacitive and thermoresistive effects	Pressure: 0.7 kPa^{-1}; Temperature: 0.83%/℃	Yes (98.5%)	(14)
	Temperature /strain	Resistance	BP/LEG on SEBS	Thermoresistive effect	Temperature: 0.1736 %/℃ Strain: 2765	No	(16)
	Pressure/temperature	Luminescence intensity; Resistance	ZnS-CaZnOS/PEDOT:PSS	Mechanoluminescent and thermoresistive effect	Pressure: - Temperature: -0.6%/℃	Yes	(6)
	Pressure/temperature	Resistance	CNF	Piezoresistive and thermoresistive effects	Pressure: -0.96 kPa^{-1}; Temperature: -2.44 %/℃	Yes	(29)
	Pressure/temperature	Resistance; voltage	PVA/NaCl/Glycerol	Potentiometric effect	Temperature: ≈14.9 mV/℃; Pressure: 278 mV/N	Yes	(36)
	Pressure/Temperature	Voltage; current	PTFE/AgNWs/PDMS	Piezoresistive and thermoresistive effects	Pressure: 15.22 kPa^{-1}; Temperature: 0.032 mV/℃	Yes	(20)
	Pressure/temperature	Voltage	PTFE/Graphene/PVDF	Triboelectric, piezoelectric, and pyroelectric	Pressure:0.092 V/kPa; Temperature: 0.11 V/℃	Yes	(34)

				effects			
	Pressure/temperature	Voltage; current	Interlocked microstructure of P(VDF-TrFE)	Localized ferroelectric polarization	Pressure: 2.2 V kPa^{-1}; Temperature: 0.27 nA/°C	Yes	(22)
	Pressure/temperature	Resistance; voltage	PAM/$BaTiO_3$/PTFE	Piezoresistive, piezoelectric, and triboelectric effects	Strain: 4.58; Pressure: 7.91 V/N	No	(30)
	Pressure/temperature	Current; voltage	P(VDF-TrFE)	Triboelectric and pyroelectric effects	Pressure: 40 nA/kPa; Temperature: 0.38 nA/°C	Yes	(13)
Trimodal	Tension/pressure/temperature	Visual color; Resistance; Capacitance	PAAM/C_{12}DMAO-PAAM/PAAM	Structural color; thermoresistive and capacitive effects	Strain: 1.4 (GF) and 1.9 nm/% Pressure: - Temp.: -	No	(31)
	Strain/pressure/temperature	Resistance; capacitance	Fe^{3+}/PAA-PVA	Thermoresistive and capacitive effects	Strain: 0.12 (GF) Pressure: 0.018 kPa^{-1}	No	(18)
	Pressure/strain/temperature	I-V; resistance; voltage; visual signal	Silicon rubber; PEDOT:PSS; AgNWs; Thermochromic molecule	Colorimetric and triboelectric effects	Pressure: 138 kPa^{-1}; Strain: 151.1;	No	(27)
	Strain/temperature/glucose	Resistance; capacitance	Zwitterionic carboxyl	Thermoresistive and capacitive	Strain: 0.0044; Sensitivity	Yes	(55)

			betaine/NIPAAm/MPBA	effects	of Glu:0.047		
	Strain/temperature/pressure	Wavelength; resistance; voltage	Fe_3O_4@C in gelatin/PVA/PDMS	Mechanochromic, thermoresistive and triboelectric effects	Strain: 2.3 nm/%; Temperature: 20.44 %/°C; Pressure: 528.0 V/kPa.	Yes (98%)	This work

References

[S1] X. Q. Wang, C. F. Wang, Z. F. Zhou, S. Chen, *Adv Opt Mater* **2014**, 2, 652.

[S2] Z. K. Liu, Y. Zheng, L. Jin, K. L. Chen, H. Zhai, Q. Y. Huang, Z. D. Chen, Y. P. Yi, M. Umar, L. L. Xu, G. Li, Q. W. Song, P. F. Yue, Y. Li, Z. J. Zheng, *Adv. Funct. Mater.* **2021**, 31, 2007622.

[S3] W. K. Lin, B. Wang, G. X. Peng, Y. Shan, H. Hu, Z. B. Yang, *Adv. Sci.* **2021**, 8, 2002817.

[S4] Q. D. Zhu, K. Van Vliet, N. Holten-Andersen, A. Miserez, *Adv. Funct. Mater.* **2019**, 29, 1808191.

[S5] Y. Xie, Y. Meng, W. X. Wang, E. Zhang, J. S. Leng, Q. B. Pei, *Adv. Funct. Mater.* **2018**, 28, 1802430.